Article

Cell Reports

Phosphoglycerate Mutase 1 Activates DNA Damage Repair via Regulation of WIP1 Activity

Graphical Abstract

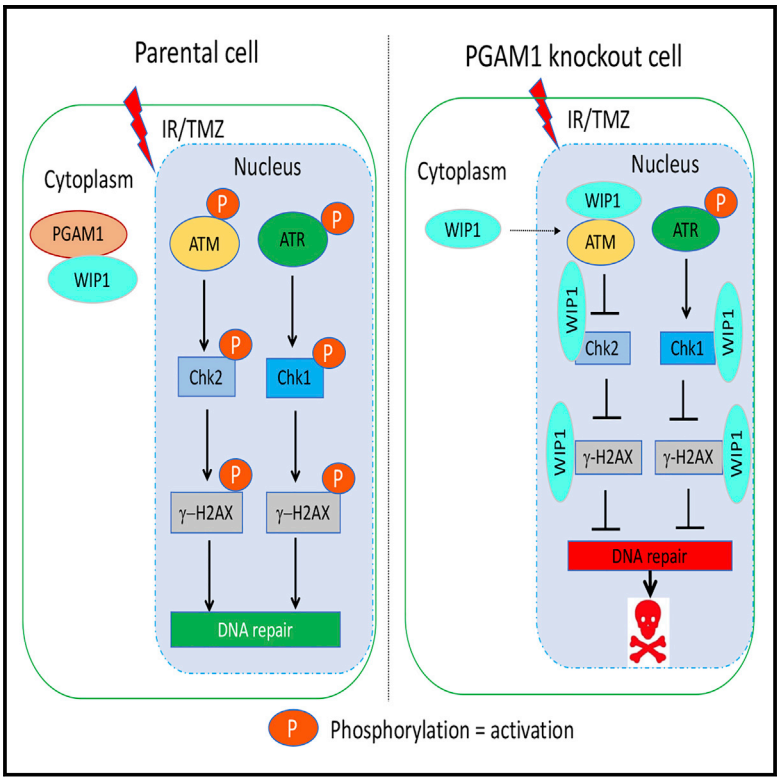

Highlights

- Overexpressed PGAM1 in gliomas sequesters the WIP1 phosphatase in the cytoplasm
- PGAM1 prevents nuclear translocation and deactivation of DNA damage repair by WIP1
- Blocking PGAM1:WIP1 binding restores WIP1 localization to deactivate ATM signaling
- Silencing of PGAM1 improves therapeutic outcome of IR and TMZ in gliomas

Authors

Shigeo Ohba,
Tor-Christian Aase Johannessen,
Kamalakar Chatla, Xiaodong Yang,
Russell O. Pieper, Joydeep Mukherjee

Correspondence

joydeep.mukherjee@ucsf.edu

In Brief

Ohba et al. show that overexpressed PGAM1 in gliomas binds to the cytoplasmic phosphatase WIP1 and prevents its nuclear translocation and dephosphorylation of the ATM signaling pathway. Silencing PGAM1 releases WIP1 to translocate to the nucleus, resulting in a decrease in ATM signaling and an increase in therapeutic efficacy of irradiation and chemotherapy in glioma.

Ohba et al., 2020, Cell Reports *31*, 107518
April 14, 2020
https://doi.org/10.1016/j.celrep.2020.03.082

CellPress

Cell Reports
Article

Phosphoglycerate Mutase 1 Activates DNA Damage Repair via Regulation of WIP1 Activity

Shigeo Ohba,[1,2,4] Tor-Christian Aase Johannessen,[1,3,4] Kamalakar Chatla,[1,5] Xiaodong Yang,[1] Russell O. Pieper,[1] and Joydeep Mukherjee[1,6,*]

[1]Department of Neurological Surgery, University of California, San Francisco, San Francisco, CA 94158, USA
[2]Department of Neurosurgery, Fujita Health University, Toyoake, Aichi, Japan
[3]Department of Biomedicine, University of Bergen, Jonas Lies Vei 91, 5009 Bergen, Norway
[4]These authors contributed equally
[5]Present address: Department of Integrative Biology, VLSB, University of California, Berkeley, Berkeley, CA 94720, USA
[6]Lead Contact
*Correspondence: joydeep.mukherjee@ucsf.edu
https://doi.org/10.1016/j.celrep.2020.03.082

SUMMARY

The metabolic enzyme phosphoglycerate mutase 1 (PGAM1) is overexpressed in several types of cancer, suggesting an additional function beyond its established role in the glycolytic pathway. We here report that PGAM1 is overexpressed in gliomas where it increases the efficiency of the DNA damage response (DDR) pathway by cytoplasmic binding of WIP1 phosphatase, thereby preventing WIP1 nuclear translocation and subsequent dephosphorylation of the ATM signaling pathway. Silencing of PGAM1 expression in glioma cells consequently decreases formation of γ-H2AX foci, increases apoptosis, and decreases clonogenicity following irradiation (IR) and temozolomide (TMZ) treatment. Furthermore, mice intracranially implanted with PGAM1-knockdown cells have significantly improved survival after treatment with IR and TMZ. These effects are counteracted by exogenous expression of two kinase-dead PGAM1 mutants, H186R and Y92F, indicating an important non-enzymatic function of PGAM1. Our findings identify PGAM1 as a potential therapeutic target in gliomas.

INTRODUCTION

Transformation of normal cells into rapidly proliferating cancer cells requires alterations of cell cycle checkpoints that act to regulate cellular proliferation (Hartwell and Kastan, 1994). DNA damage repair (DDR) is one of the major pathways that prevent normal cells from transforming into cancer cells. In normal cells, the DDR pathway is activated upon exposure to agents that induce DNA damage that require repair. The DDR pathway is deactivated once the DNA repair process is complete (Kim and Haber, 2009); if the DNA lesion cannot be repaired, the cell undergoes cellular senescence or apoptosis. In cancer cells, however, the pathway is constitutively active. Current cancer treatments, such as irradiation (IR) and chemotherapy, attempt to induce DNA lesions to levels that surpass the ability of the cell to repair all of the DNA damage, ultimately leading to cell death (Curtin, 2013). Cancer cells, however, are often efficient in repairing the DNA damage and thus can avoid senescence and cell death.

Recent findings suggest that cellular metabolism is altered in cancer cells in order to support the needs of indefinite proliferation by performing functions that are not fully understood (DeBerardinis and Chandel, 2016; Pavlova and Thompson, 2016). Several enzymes in the glycolytic pathway, such as hexose kinase II (HKII), pyruvate kinase-M2 (PKM2), phospho-fructo kinase (PFK), enolase, and phosphoglycerate mutase (PGAM1), are aberrantly overexpressed in cancer cells (Wolf et al., 2011; Mukherjee et al., 2013, 2016; Capello et al., 2011; Vander Heiden et al., 2010). PGAM1 converts 3-phosphoglycerate (3-PG) into 2-phosphoglycerate (2-PG) using phospho-histidine11 as a phosphate donor/acceptor site within its catalytic domain through formation of a 2,3-bisphosphoglycerate intermediate (Vander Heiden et al., 2010; Hitosugi et al., 2012). PGAM1 is expressed at various levels within various normal tissues during cellular differentiation or transformation (Jiang et al., 2014). Furthermore, PGAM1 is overexpressed in several types of cancer, including gliomas (Sanzey et al., 2015; Liu et al., 2018).

PGAM1 is unique among the glycolytic enzymes in that its transcription is regulated by the tumor suppressor p53 (Cheung and Vousden, 2010), and increased expression of PGAM1 has been reported to immortalize primary cells through an unknown mechanism (Kondoh et al., 2005). Cancer cells that express PKM2 have increased levels of phosphorylated PGAM1 at residue histidine11, which leads to increased mutase activity and results in increased production of PEP. This positive feedback loop of PEP production and enzymatic activity of PGAM1 may act as an alternate route to funnel more metabolites into the biosynthetic arm of the glycolysis pathway (Vander Heiden et al., 2010). The benefit of PGAM1 overexpression was attributed toward increased glycolysis and biosynthesis via the pentose phosphate pathway (PPP), thereby promoting cancer cell proliferation and tumor growth that can be reversed using genetic and pharmacological approaches to inhibit PGAM1 activity (Hitosugi et al., 2012). Previously, a chemical genomics screen identified the compound MJE3 as a non-specific target of PGAM1 that inhibits PGAM1 enzyme activity and breast cancer cell growth (Evans et al., 2005). Detailed biochemical analysis

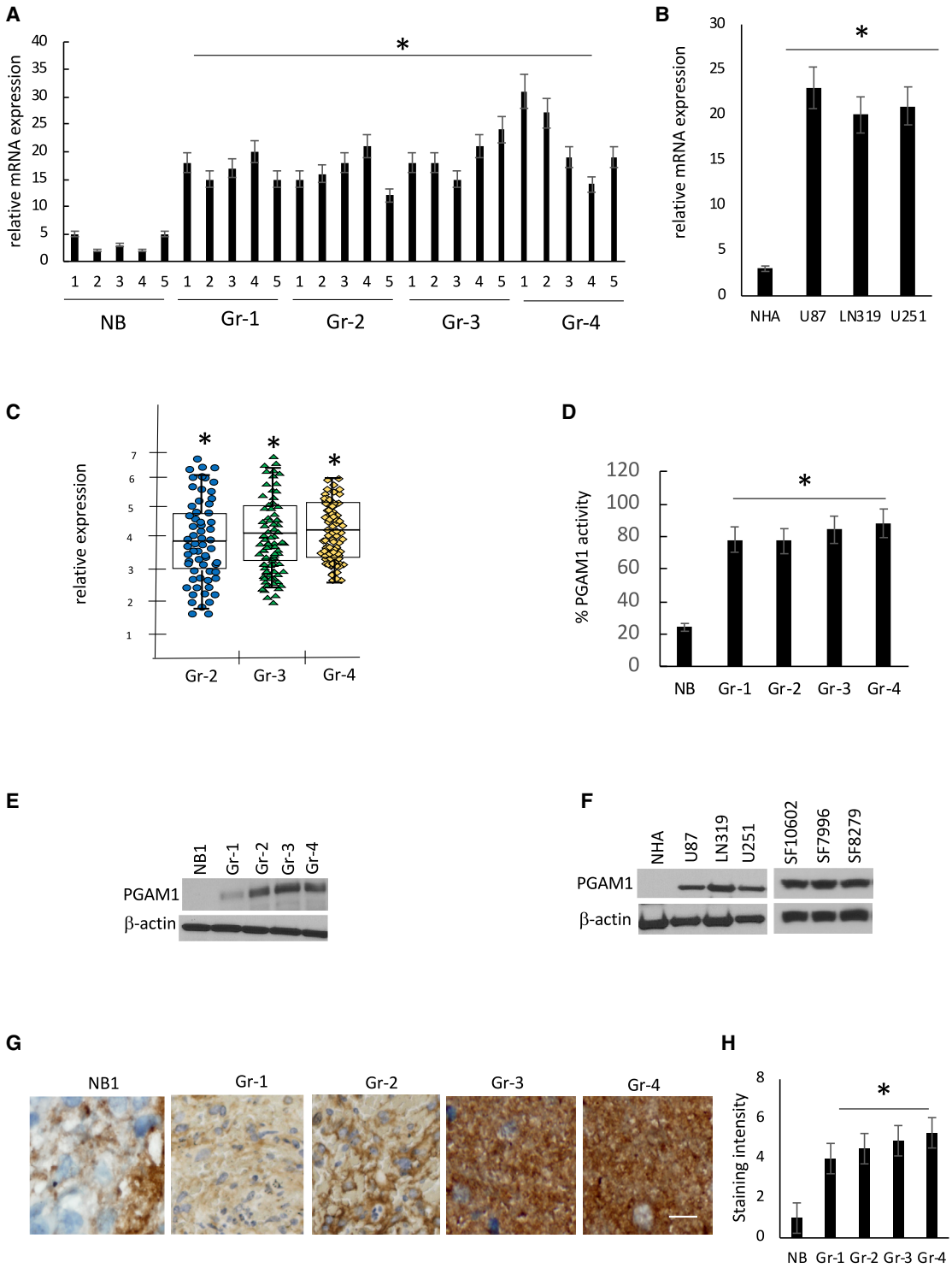

Figure 1. PGAM1 Is Overexpressed in Gliomas

(A) Triplicate quantitative PCR analysis of the level of PGAM1 transcripts in human non-neoplastic normal brain (NB) and grade I (Gr-1), grade II (Gr-2), grade III (Gr-3), and grade IV (Gr-4) astrocytomas; n = 5 for each group numbered 1–5.

(B) Triplicate quantitative PCR analysis of the level of PGAM1 transcripts in normal human astrocytes (NHAs) and three glioma cells lines, U87, LN319, and U251.

(C) TCGA-based analysis of PGAM1 mRNA levels in grade II (Gr-2), grade III (Gr-3), and grade IV (Gr-4) astrocytomas relative to normal brain controls (1.0 on the y axis).

(legend continued on next page)

revealed that Y26 phosphorylation of PGAM1 leads to increased activation by releasing E19 from the active site, which stabilizes binding of cofactor 2,3-bisphosphoglycerate and H11 phosphorylation (Hitosugi et al., 2013).

Recent studies have demonstrated that PGAM1 enzyme activity also has a non-metabolic role in homologous recombination (HR)-mediated DDR. PGAM1 enzyme activity regulates stability of CTBP-interacting protein (CtIP), a HR component that mediates replication protein A recruitment and Rad51 filament formation (Qu et al., 2017). On the other hand, enzymatically dead PGAM1 demonstrated interesting non-metabolic function by promoting cancer metastasis. PGAM1 interacts with α-smooth muscle actin (ACTA2) and thereby modulates actin filaments assembly, cell motility, and cancer cell migration independent of its metabolic activity. Enzymatically inactive H186R mutant PGAM1 can bind ACTA2, whereas metabolically active, 201–210 amino acid-deleted PGAM1 cannot. In a xenograft model, decreased metastasis was observed with PGAM1 loss and was found to be prognostic in human breast cancer patients along with ACTA2 (Zhang et al., 2017).

Here we report that PGAM1 is overexpressed in human gliomas across all grades (I–IV) and in established glioma cell lines. This overexpression of PGAM1 indirectly increases the efficiency of DDR and increases resistance to IR and temozolomide (TMZ) treatment. In addition, we show that PGAM1 traps WIP1 in the cytoplasm, thereby controlling phosphorylation of major cell cycle checkpoint proteins, such as ATM, Chk1, Chk2, and γ-H2AX. Together, these data suggest that PGAM1 inhibitors that block its interaction with WIP1 are ideal candidates to sensitize cells against DNA-damaging therapeutic agents.

RESULTS

PGAM1 Is Overexpressed in Human Glioblastoma (GBM) along with PGAM1 Activity

To determine if PGAM1 is expressed in primary brain tumors, we examined RNA levels of PGAM1 in human gliomas (grades I–IV) and normal brain obtained from frozen and formalin-fixed tissue samples. Real-time PCR gene expression analysis was performed with two independent sets of primers. As shown in Figure 1A, PGAM1 is overexpressed almost 4-fold in grade I tumors compared with normal brain, suggesting that overexpression of PGAM1 consistently occurs in gliomas from histologic grades I to IV. World Health Organization (WHO) grade III and IV gliomas express a small but statistically significant increase in PGAM1 expression compared with grade I tumors that is almost 5-fold overexpressed compared with normal brain. To find an *in vitro* model that resembles the PGAM1 overexpression found in human tumors, we examined three established glioma cell lines and compared them with normal human astrocytes (NHAs) using the same real-time PCR assay. Similar to primary human tumors, established glioma cell lines showed an almost 3.5- to 4-fold increase in PGAM1 expression compared with NHAs (Figure 1B). Similarly, The Cancer Genome Atlas (TCGA) dataset analyses demonstrated overexpression of PGAM1 compared with normal brain in grade II–IV gliomas (Figure 1C). To determine if the changes in PGAM1 expression noted at the RNA level were reflected in PGAM1 activity and protein expression, fixed material and lysates from frozen samples used for RNA analysis were subjected to a biochemical assay (to measure enzyme activity), western blot, and immunohistochemical analysis. As demonstrated by the biochemical assay, low-PGAM1-expressing normal brain samples exhibited low levels of PGAM1 enzyme activity, while the PGAM1 enzyme activity of the glioma samples correlated well with increased expression of the PGAM1 tumor mRNA (Figure 1D). As shown in the western blots in Figure 1E, representative normal brain samples expressed significantly less PGAM1 protein than brain tumor samples or commonly used glioma cell lines and three primary glioma stem-like cells (GSCs) established at the University of California, San Francisco (UCSF) (Fouse et al., 2014; Mancini et al., 2018; Figure 1F). These results were consistent with immunohistochemical analyses of fixed tissue (Figure 1G), where semiquantitative analysis (Figure 1H) showed, as noted at the RNA level, that normal brain expresses low levels of PGAM1 protein compared with tumor samples.

Reductions in PGAM1 Expression Sensitize GBM Cell Lines to IR and TMZ Treatment

Upregulation of PGAM1 may be an early event in tumorigenesis, suggesting that PGAM1 is critical for glioma growth. To address this possibility, we modulated the expression of PGAM1 and monitored the effect on *in vitro* and *in vivo* growth of these cells. For these studies, U87, LN319, SF10602, and SF7996 glioma cells were used, as these cells demonstrate similar levels of PGAM1 mRNA and protein compared with human glioma samples (Figures 1B and 1F). Because all analyzed astrocytomas upregulate PGAM1, and because suppression of PGAM1 levels have been shown to inhibit tumor cell growth in other systems (Hitosugi et al., 2012; Evans et al., 2005), we first examined the consequences of PGAM1 knockdown in GBM cells. As shown in the western blot in Figure 2A, the lentiviral introduction of two different short hairpin RNAs (shRNAs) targeting PGAM1 resulted in two independent populations of GBM cells for each cell line, each of which exhibited significant decreases in PGAM1 expression compared with parental and

(D) PGAM1 activity (mean + standard error [SE]) determined using an assay coupled to the oxidation of NADH in normal brain (NB) and grade I (Gr-1), grade II (Gr-2), grade III (Gr-3), and grade IV (Gr-4) astrocytomas; N = 5 for each group were measured.

(E) Western blot verification of PGAM1 and β-actin protein levels in human normal brain (NB-1) and grade I (Gr-1), grade II (Gr-2), grade III (Gr-3), and grade IV (Gr-4) astrocytomas.

(F) Western blot verification of PGAM1 and β-actin protein levels in normal human astrocytes (NHAs) and glioma cells lines U87, LN319, U251, SF10602, SF7996, and SF8279.

(G) Immunohistochemistry (IHC) analysis of representative fixed sections from tumors in (A) using PGAM1 antibody (bar, 100 μM).

(H) Semiquantitative analysis (four-tiered scale) of IHC staining; N = 4 (NB), 5 (Gr-1), 9 (Gr-2), 11 (Gr-3), and 10 (non-segregated Gr-4). All tumor PGAM1 values were significantly larger than NB values ($p < 0.05$).

Except where noted, all values were derived from three independent experiments ± SD. *$p < 0.05$.

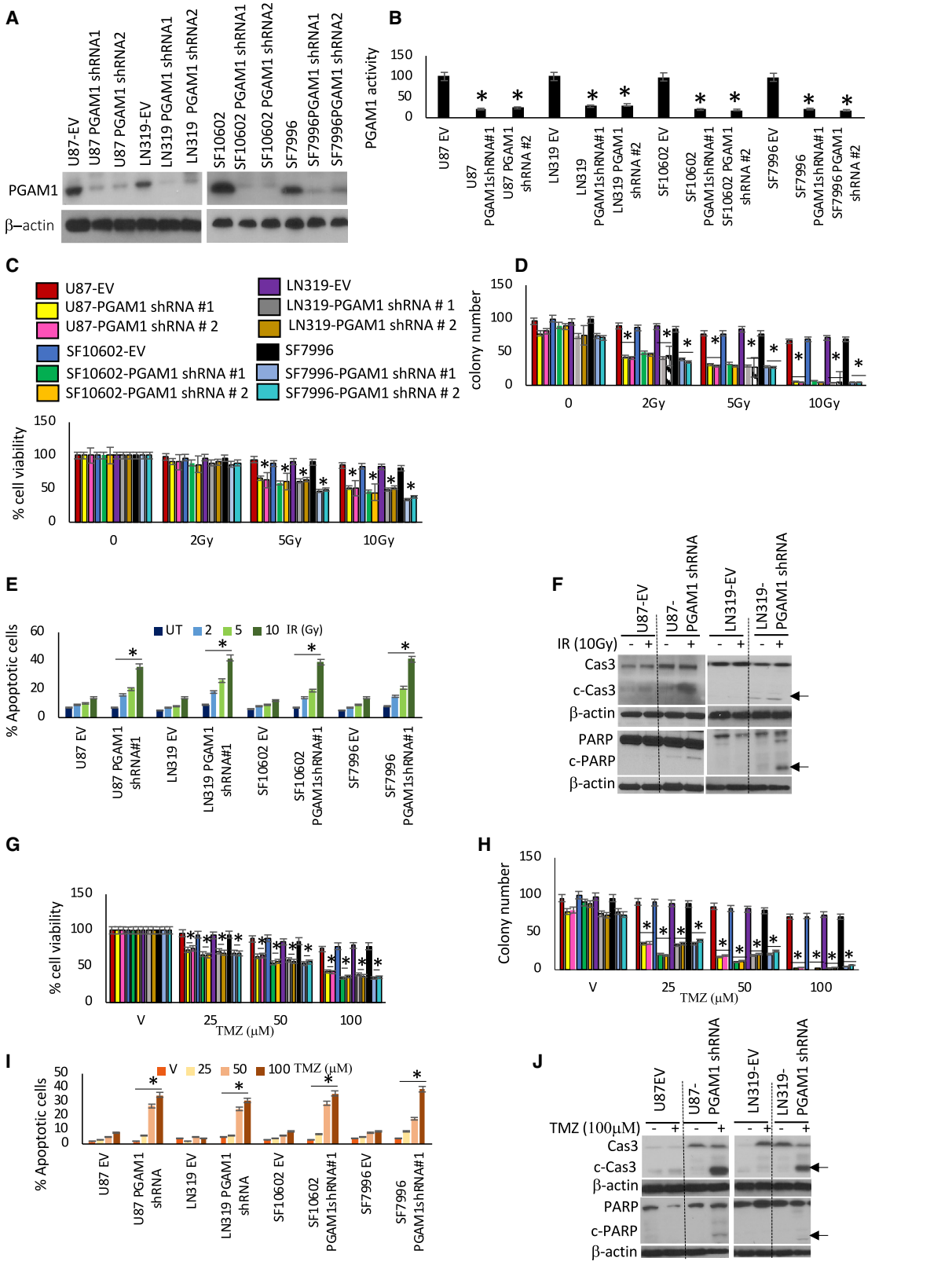

(legend on next page)

empty vector controls. Decreased PGAM1 expression was associated with a significant decrease in PGAM1 activity (Figure 2B). In contrast to previously published data, PGAM1 suppression did not affect proliferation or colony formation (Figures 2C and 2D) in any of the glioma cell lines. Interestingly, when these PGAM1-knockdown cells were treated with IR and TMZ, they showed significantly increased sensitivity compared with the parental cells in terms of cell viability (Figures 2C and 2G) and apoptosis (Figures 2E and 2I; Figures S1A and S1B). Moreover, these cells formed significantly fewer colonies (Figures 2D and 2H) than the parental cells. However, in contrast to glioma cells, NHAs expressed low levels of PGAM1 and were more susceptible to both IR and TMZ, which did not further increase by PGAM1 silencing (Figures S1C and S1D), and western blot analysis demonstrated the presence of cleaved caspase-3 and cleaved PARP in PGAM1-knockdown cells treated with IR and TMZ, consistent with induction of apoptosis (Figures 2F and 2J). To mimic genetic loss, we used pharmacological inhibitors (PGAM-tide and Alizarin) that block PGAM1 enzyme activity (Hitosugi et al., 2012; Engel et al., 2004; Figure S1E), but surprisingly this had no effect on cell viability or apoptosis when combined with IR (Figures S1F and S1G) and TMZ (Figures S1H and S1I) treatment.

Loss of PGAM1 Decreases DNA Damage Repair Pathway Activation Despite the Presence of DNA Damage after IR and TMZ Treatment

IR and TMZ treatment induce the formation of double-strand DNA breaks and activation of the DDR pathway. We therefore wanted to investigate if PGAM1 loss sensitizes GBM cells to IR and TMZ treatment through regulation of the DDR pathway. PGAM1-knockdown cells were subjected to IR and TMZ treatment, and double-strand breaks were measured using a single-cell comet assay performed under neutral pH conditions. In the control cells, fragmented DNA resulting from the double-strand breaks decreased over time, whereas fragmented DNA remained elevated in PGAM1-knockdown cells. After ionizing radiation treatment (10 Gy) in parental cells, the maximum number of double-strand breaks was found after 24 h and began gradually decreasing by 72 h. In PGAM1-knockdown cells, the number of double-strand DNA breaks remained unchanged from 24 h for up to 7 days (Figure 3A). Similarly, after TMZ (100 μM) treatment in parental cells, the maximum number of double-strand breaks was detected after 72 h and then gradually declined, whereas it remained elevated in PGAM1-knockdown cells for up to 7 days (Figure 3B). Previously identified PGAM1 interactors such as CtIP and ACTA2 had no significant effect on the extent of DNA damage or the repair of DNA breaks, as demonstrated by small interfering RNA (siRNA)-mediated knockdown followed by IR (10 Gy) treatment and comet assay (Figure S2A). But as expected, treatment with IR (10 Gy) resulted in formation of γ-H2AX foci (a surrogate measure of double-strand DNA breaks) in parental U87 and LN319 cells at day 1, which gradually decreased on days 5 and 7, indicating efficient repair of DNA damage (Figure 3C). Very few γ-H2AX foci were observed in U87 and LN319 PGAM1-knockdown cells after IR treatment, which did not change significantly over time (day 3 versus day 5 versus day 7) (Figure 3C). Similarly, 3 h exposure of parental cells to TMZ (100 μM) resulted in formation of γ-H2AX foci beginning 2 days after drug treatment, with a gradual decrease at days 5 and 7. Contrary to the parental cells, few γ-H2AX foci were observed in PGAM1-knockdown cells after TMZ treatment, which remained unchanged over time (Figure 3D). At early time points, DNA breaks are infrequent until 12 h (Figure S2B). Notably, NHAs treated with IR and TMZ showed significantly higher level of DNA breaks compared to the parental glioma cells and the DNA breaks in the NHAs were not similarly resolved with time (Figure S2C). PGAM1 knockdown in NHAs did not provide any significant additive changes in the extent of DNA breaks and γ-H2AX foci formation (Figures S2C and S2D).

Response to DNA damage is related to DDR efficiency, and HR has previously been reported to be altered upon suppression of PGAM1 (Qu et al., 2017). We therefore looked at HR and non-homologous end joining (NHEJ) efficiency by using a plasmid-based system using the ATM kinase inhibitor KU-55933 and DNA ligase-4 inhibitor SCR-7 as a positive control for HR and NHEJ inhibition. However, no change in HR or NHEJ efficiency was observed in parental or PGAM1-knockdown cells (Figure S2E), whereas KU-55933 and SCR-7 significantly lowered HR and NHEJ efficiency, respectively. This suggests that suppression of PGAM1 does not regulate HR and NHEJ efficiency in gliomas.

Figure 2. Knocking Down PGAM1 Increases Sensitivity toward Ionizing Radiation (IR) and TMZ in Glioma Cell Lines

(A) Parental established U87, LN319, and stem-like SF10602 and SF7996 glioma cells were infected with lentivirus containing empty vector (EV) or one of the two shRNAs targeting PGAM1 (PGAM1 shRNA#1 and PGAM1 shRNA#2) and were then established and analyzed using western blot for levels of PGAM1 and β-actin.

(B) PGAM1 activity (mean + SE) was determined in triplicate for each group using an assay coupled to the oxidation of NADH.

(C) Glioma cells from (A) were treated with and without ionizing radiation (IR; 10 Gy), and cell viability was determined on day 5 using alamarBlue assay. Values are the mean of three independent experiments performed in triplicate.

(D) Number of colonies (>50 cells) that arose 28 days following plating of the cells from (C) in soft agar.

(E) Apoptosis of glioma cells from (C) was measured using annexin V staining and flow cytometry assay after 3, 5, or 7 days of treatment.

(F) Western blot analysis for cleaved caspase-3 and PARP in U87 and LN319 glioma cells from (C). The cleaved 19 and 17 kDa caspase-3 protein bands and PARP bands are marked with arrows.

(G) Glioma cell populations from (A) were treated with and without TMZ (100 μM) for 5 days, and cell viability was determined using alamarBlue assay. Values are the mean of three independent experiments performed in triplicate.

(H) Number of colonies (>50 cells) that arose 28 days following plating of the cells from (G) in soft agar.

(I) Apoptosis of glioma cells from (G) were measured using annexin V staining and flow cytometry assay after 3, 5, or 7 days of treatment.

(J) Western blot analysis for cleaved caspase-3 and PARP in U87 and LN319 glioma cells from (G). The cleaved 19 and 17 kDa caspase-3 protein bands and PARP bands are marked with arrows.

Except where noted, all values were derived from three independent experiments ± SD. *$p < 0.05$.

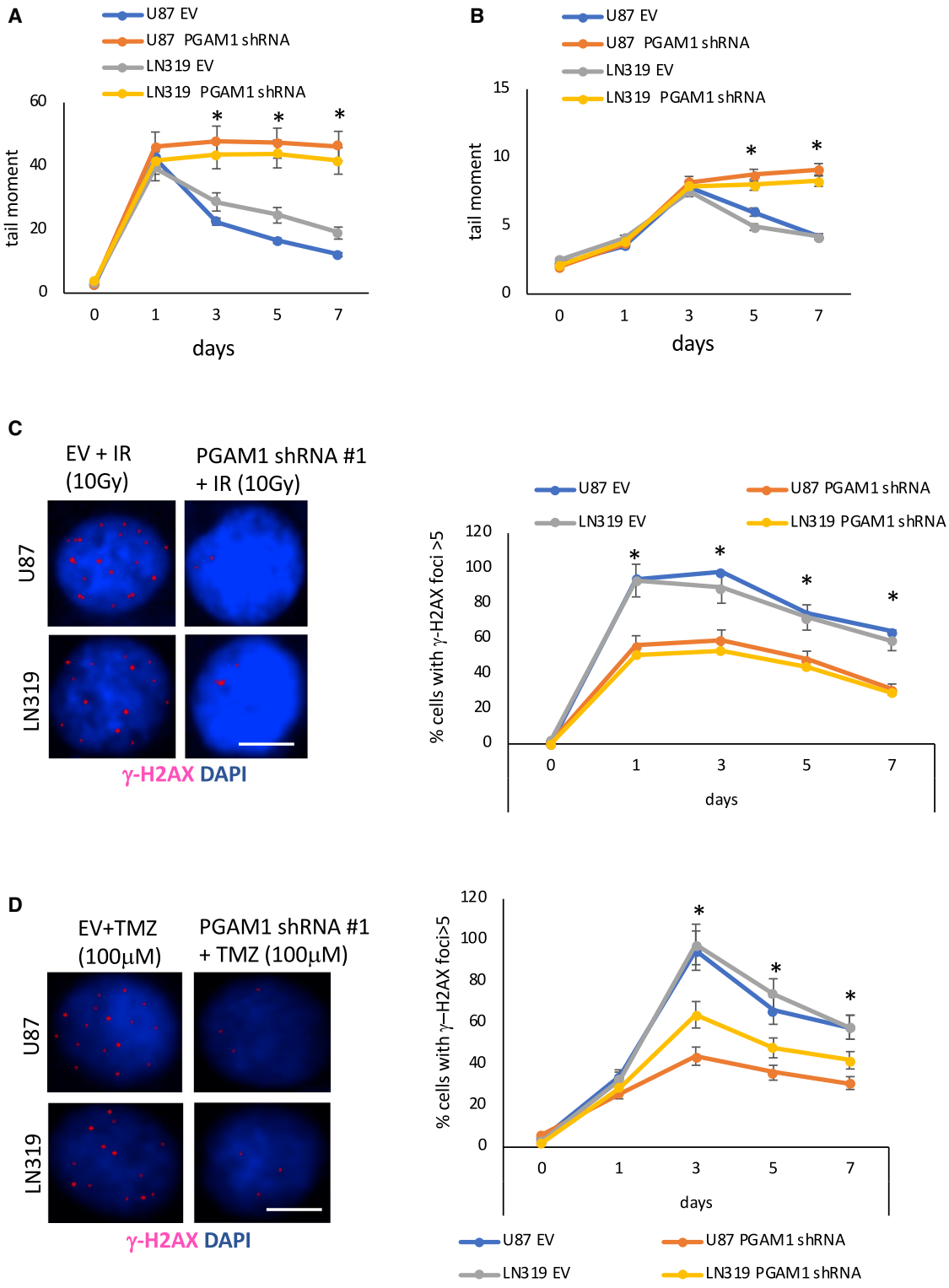

Figure 3. Loss of PGAM1 Decreases DDR Pathway Activation despite the Presence of DNA Damage after Radiation and TMZ Treatment

(A and B) Analysis of tail moment (a measure of DNA fragmentation) in cells from Figure 2A treated with IR (10 Gy) (A) and (B) treated with TMZ (100 μM) before being harvested after 0, 1, 3, 5, and 7 days. Each data point represents the mean + SE of at least 100 cells per treatment.

(C and D) Representative photomicrographs of cells from Figure 2A treated with IR (10 Gy) (C) and (D) TMZ (100 μM) and subsequently analyzed for phospho-γ-H2AX foci (a measure of DNA double-strand break) by immunofluorescent staining with anti-Ser-139-phosphorylated H2AX antibody (in red) and counterstained

(legend continued on next page)

Loss of PGAM1 Inhibits Phosphorylation of ATM and Downstream Signaling

ATM is one of the major kinases involved in the cellular response to DNA double-strand breaks, which may arise through the collapse of stalled replication forks or through exposure to DNA-damaging agents. Autophosphorylation of ser1981 is a reliable marker of ATM activation (Curtin, 2013). We therefore treated U87 and LN319 cells with IR and TMZ, and performed western blotting to determine whether ATM phosphorylation would differ on the basis of PGAM1 expression. Phosphorylation of ATM ser1981 was readily observed in parental U87 and LN319 cells after both IR (10 Gy) and TMZ (100 μM) treatment as expected 48 h post-treatment (Figure 4A). At earlier time points before 48 h, no change in phosphorylation of ATM ser1981 was observed (Figure S3A). In contrast, phosphorylation of ATM ser1891 was not observed in PGAM1-knockdown U87 and LN319 cells after IR or TMZ treatment, indicating lack of ATM activation in these cell populations (Figure 4A). Moreover, in parental cells, IR treatment activated ATM and downstream signaling, as observed by phosphorylation of Chk2 at thr68 and cdc25C at ser216. However, phosphorylation of Chk2 thr68 or cdc25 ser216 was not observed in PGAM1-knockdown cells, which is consistent with deficient ATM signaling. TMZ treatment in parental cells resulted in phosphorylation of Chk1(ser345), Chk2(thr68), and cdc25C(ser216), which was not observed in PGAM1-knockdown cells. Consequently, as PGAM1-knockdown cells demonstrated loss of activating phosphorylation of Chk1 and Chk1, we found significantly increased G2/M arrest followed by apoptosis in response to IR and TMZ compared with corresponding parental cells (Figure 4B). To determine if PGAM1 knockdown affects the protein kinase ATR, an ATR kinase assay was performed on corresponding PGAM1-proficient and PGAM1-deficient cells. Phosphorylation of Chk1 in parental cells paralleled the activation of ATR, as demonstrated by the presence of serine/threonine phosphorylation of the ATR substrate PHAS by ATR immunoprecipitates of TMZ-treated cells. In contrast, in TMZ-treated PGAM1-knockdown cells, ATR activation was observed, but there was no activation of Chk1, as demonstrated by lack of Chk1 ser345 phosphorylation (Figure 4C). Our observations collectively indicate that PGAM1 expression is necessary for ATM downstream signaling in response to IR and TMZ in glioma cells.

PGAM1 Influences WIP1 Cytoplasmic Localization

Because PGAM1 is mainly a cytoplasmic protein and may not be directly regulating dephosphorylation of nuclear DDR proteins, we next looked at proteins that shuttle between the cytoplasm and nucleus and play roles in regulating phosphorylation of DDR proteins. We selected five proteins (PP1, PP2A, PP4, PP6, and WIP1) and examined the effect of PGAM1 knockdown on the localization of these five proteins using immunofluorescence analysis. Only WIP1, which was located predominantly in the cytoplasm of control cells (Figure 4D), shifted to the nucleus in PGAM1-knockdown cells in response to DNA damage. The other four proteins (PP1, PP2A, PP4, and PP6) did not show any changes in their cellular localization due to loss of PGAM1 in either cell line (Figure 4D). Moreover, no change in subcellular localization or induction of PGAM1 protein expression was observed with IR or TMZ treatment (Figure 4E). These results therefore suggest that loss of PGAM1 expression allows increased export of WIP1 to the nucleus. Consequently, a shift in WIP1 localization from the cytoplasm to the nucleus was observed in PGAM1-knockdown cells using co-immunofluorescence analysis (Figure 4F). To determine the status of WIP1 protein expression in human glioma samples and cells lines, we studied the matched samples that have been used previously for PGAM1 expression analysis. A uniform WIP1 expression was detected in normal brain, normal astrocytes, glioma cell lines, and human glioma tumor samples (Figure S3B). Moreover, we analyzed WIP1 RNA expression using real-time PCR analysis and found no significant difference in RNA expression in gliomas compared with normal brain (Figure S3C). Similarly, U87 and LN319 expressed physiological levels of WIP1 (compared with the WIP1-overexpressing cell lines Lncap and MCF7), and there was no change in expression of WIP1 upon PGAM1 knockdown (Figure S3D).

PGAM1 Physically Binds WIP1 in the Cytoplasm

As WIP1 is a phosphatase found in the cytoplasm in the presence of PGAM1, we hypothesized that PGAM1 binds WIP1 to block WIP1-mediated interactions with ATM, Chk1, Chk2, and γ-H2AX. We therefore tested whether PGAM1 directly interacts with WIP1 to restrict movement toward the nucleus by performing immunoprecipitation and reverse immunoprecipitation using antibodies specific for PGAM1, WIP1, ATM, Chk1, Chk2, and γ-H2AX. In control cells, PGAM1 was detected in WIP1 immunoprecipitates, and WIP1 was detected in PGAM1 immunoprecipitates (Figure 5A; Figure S4A). Moreover, cell fractionation analysis revealed that PGAM1:WIP1 interaction is present only in the cytoplasmic fraction (Figure 5B), whereas no other phosphatases (PP1, PP2A, PP4, or PP6) were found to be immunoprecipitated with PGAM1 antibody (Figure S4B). In PGAM1-knockdown cells, PGAM1 was not detected in WIP1 immunoprecipitates, and WIP1 was accordingly not detected in PGAM1 immunoprecipitates (Figure 5C; Figures S4C and S4D). When the WIP1 antibody was used in PGAM1-knockdown cells, ATM, Chk1, Chk2, and γ-H2AX were all detected in WIP1 immunoprecipitates (Figure 5C; Figure S4D). We also performed immunoprecipitation using ATM, Chk1, Chk2, or γ-H2AX antibodies separately, and WIP1 was detected in each pull-down in PGAM1-knockdown cells (Figure 5C; Figure S4D). In each separate immunoprecipitation using a specific antibody targeting a DDR protein (ATM, Chk1, Chk2, or γ-H2AX), the other DDR proteins were not detected (Figure 5C; Figure S4D). Importantly, WIP1 was not observed in control U87 and LN319 cells immunoprecipitated with ATM, Chk1, Chk2, or γ-H2AX antibodies (Figure S4E). Loss of PGAM1 expression therefore allows WIP1 to associate with key nuclear signaling proteins in the DNA damage response pathway.

with DAPI (in blue) to visualize nuclei (left panels). Quantitative analysis of phospho-γ-H2AX foci counted on >200 cells per group as indicated (right panels). The percentage of cells with phospho-γ-H2AX foci was determined in all cell populations treated with either IR (10 Gy) or TMZ (100 μM) at the indicated time points. Except where noted, all values were derived from three independent experiments ± SD. *$p < 0.05$.

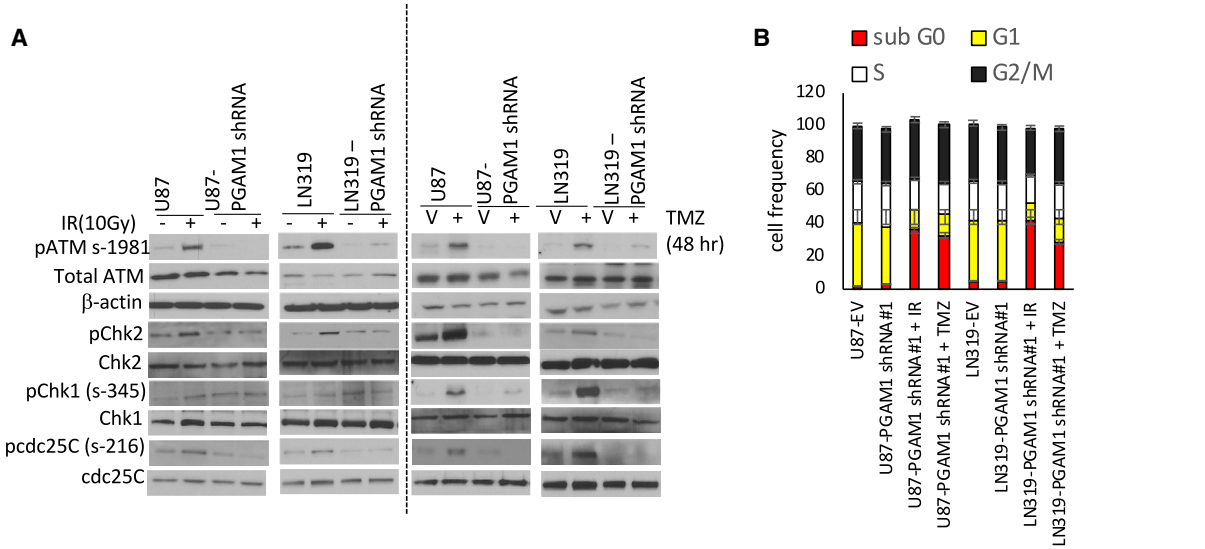

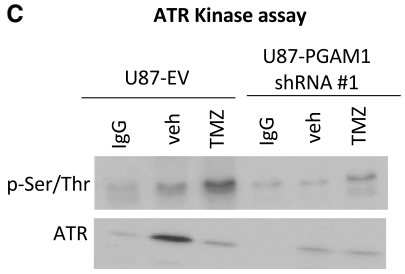

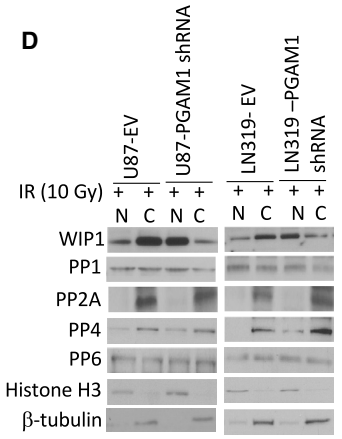

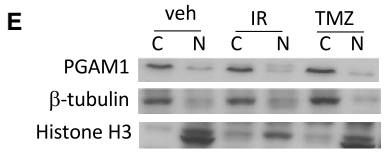

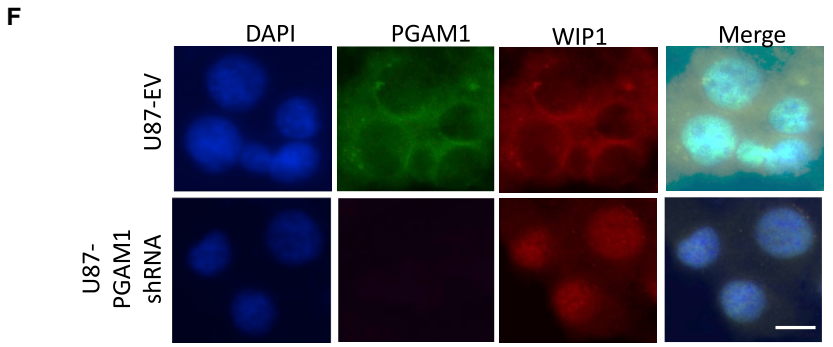

(legend on next page)

PGAM1 Binds WIP1 Independent of PGAM1 Enzymatic Activity

To understand if the metabolic enzymatic activity of PGAM1 regulates the DDR pathway, we reconstituted a kinase-dead form of PGAM1 in stable PGAM1-knockdown cells (Figure 5D) and measured PGAM1 activity, DNA damage, and γ-H2AX foci formation in U87 and LN319 cells (Figures 5E–5G). As expected, the PGAM1 enzyme activity, 3PG production, and PPP flux in cells infected with two mutant (H186R and Y92F) PGAM1 constructs were similar to those of PGAM1-knockdown cells. In contrast, the enzyme activity (Figure 5E), 3PG production, and PPP flux (Figures S5A and S5B) in cells infected with a wild-type (WT) shRNA-resistant PGAM1 construct were similar to those in parental cells. Interestingly, reduction of γ-H2AX foci formation in PGAM1-knockdown cells was rescued by introduction of either the H186R or Y92F PGAM1 mutant or WT PGAM1 constructs (Figure 5F). As observed earlier, levels of DNA damage measured by the comet tail assay were elevated and sustained in PGAM1-knockdown cells, whereas expression of the mutant forms H186R or Y92F of PGAM1 or WT PGAM1 prevented sustained levels of DNA damage (Figure 5G). Immunoprecipitation studies revealed that mutant, kinase-dead PGAM1 is capable of binding to WIP1, similar to endogenous PGAM1 (Figure 5H). This resulted in cytoplasmic localization of WIP1, as revealed by immunofluorescence staining (Figure 5I), suggesting that PGAM1 metabolic activity is not required for PGAM1-mediated regulation of the DDR pathway.

Silencing of WIP1 Reverses the Effects of PGAM1 Deficiency on IR and TMZ Resistance

Our previous results suggest that PGAM1 loss allows WIP1 to enter the nucleus and directly interact with and dephosphorylate Chk1, Chk2, ATM, and γ-H2AX, thereby leading to inactivation of the DDR pathway. We next asked whether silencing of WIP1 expression could reverse the DDR pathway inactivation in PGAM1-knockdown cells. Furthermore, we also silenced the expression of the four other previously studied proteins, PP1, PP2a, PP4, and PP6, and monitored if loss of any of them could in fact reverse the effect of DDR pathway inactivation due to PGAM1 deficiency. To test this, we transfected PGAM1-knockdown cells with pooled siRNAs targeting WIP1, PP1, PP2A, PP4, and PP6. As shown in Figure 6A, levels of WIP1 protein were depleted (almost 80%) in the WIP1 siRNA transfected PGAM1-knockdown cells. Similarly, levels of PP1, PP2A, PP4, and PP6 were about 90% depleted using the appropriate pooled siRNA in PGAM1-knockdown cells (Figure S5C). We then treated these distinct cell populations with IR (10 Gy) or TMZ (100 μM), and measured γ-H2AX foci, apoptosis, and colony formation. Treatment with IR or TMZ led to increased γ-H2AX foci formation in WIP1-deficient, PGAM1-knockdown cells, compared with WIP1-proficient, PGAM1-knockdown cells (Figures 6B and 6C). In agreement with this, fewer apoptotic cells (Figures 6D and 6E) and significantly more colonies (Figures 6F and 6G) were observed in IR (10 Gy) and TMZ (100 μM) treated WIP1-deficient, PGAM1-knockdown cells compared with WIP1-proficient, PGAM1-knockdown cells. No change in γ-H2AX foci formation and apoptosis was observed in PP1, PP2A, PP4, and PP6 deficient, PGAM1-knockdown cells compared with PGAM1-knockdown cells (Figures S5C and S5D).

Loss of PGAM1 Sensitizes Gliomas to IR and TMZ Treatment *In Vivo*

To determine if the events noted *in vitro* are also observed *in vivo*, we intracranially injected mice with luciferase-labeled U87 and LN319 cells infected with viral particles that encode empty shRNA vector (EV) or PGAM1 shRNA vector. Tumor growth was monitored by bioluminescence imaging, and tumor-bearing animals were treated with or without IR or TMZ. Control EV-expressing tumors grew over a 7 week period (Figure 7A), necessitating the sacrifice of all animals by day 70 post-implantation. Importantly, tumors expressing PGAM1 shRNA exhibited a statistically significant reduction in tumor growth relative to EV-expressing tumors when treated with IR or TMZ (Figure 7A). This increased sensitivity toward IR and TMZ translated into a significant survival advantage of 30 days on average for mice with PGAM1 shRNA#1-expressing tumors (Figure 7B). Furthermore, additional growth inhibition and survival advantage was noted in animals with PGAM1-knockdown cells treated with both IR and TMZ (Figure 7B). Moreover, tumors generated from U87 cells with stable expression of catalytic inactive Y92F and H186R PGAM1 mutants in an otherwise WT PGAM1-deficient background demonstrated similar resistance to IR and/or TMZ treatment as the parental PGAM1-proficient tumors (Figure 7A). Consequently, IR/TMZ treatment did not prolong

Figure 4. Loss of PGAM1 Inhibits Phosphorylation of ATM and Controls Cellular Localization of WIP1

(A) Isogenically paired U87 and LN319 cells differing only in PGAM1 expression were untreated (−) or treated (+) with IR (10 Gy) and with vehicle (veh) or TMZ (100 μM, 3 h), and cells were harvested at 48 h for analysis of pATM (ser1981), ATM, pChk1 (ser345), Chk1, pChk2 (thr68), Chk2, pcdc25C (ser216), cdc25C, and β-actin expression by western blot.

(B) Fluorescence-activated cell sorting (FACS)-based cell cycle phase distribution analysis of glioma cells differing only in PGAM1 expression after 7 days of IR (10 Gy) treatment, DMSO, and TMZ treatment (100 μM) treatment. U87-EV and LN319-EV, untreated control; U87-PGAM1-shRNA#1 and LN319-PGAM1-shRNA#1, DMSO treated control.

(C) An ATR (or control IgG) immunoprecipitate (IP) was first prepared and incubated with the ATR substrate PHAS, after which a western blot analysis of the extent of ATR-mediated PHAS Ser/Thr phosphorylation was performed.

(D) Western blot analysis of WIP1, PP1, PP2A, PP4, and PP6 from the nuclear (N) and cytoplasmic (C) fractions of control or PGAM1 shRNA-containing U87 and LN319 cells treated once with IR (10 Gy).

(E) Western blot analysis of PGAM1 from the nuclear (N) and cytoplasmic (C) fractions of parental U87 cells treated once with drug vehicle (veh; DMSO), IR (10 Gy), and TMZ (100 μM).

(F) DAPI (blue)/PGAM1 (green)/WIP1 (red) co-immunofluorescence analysis was used to verify the subcellular localization of WIP1 in parental and PGAM1-knockdown U87 cells. Scale bars, 10 μm.

Except where noted, all values were derived from three independent experiments ± SD. * $p < 0.05$.

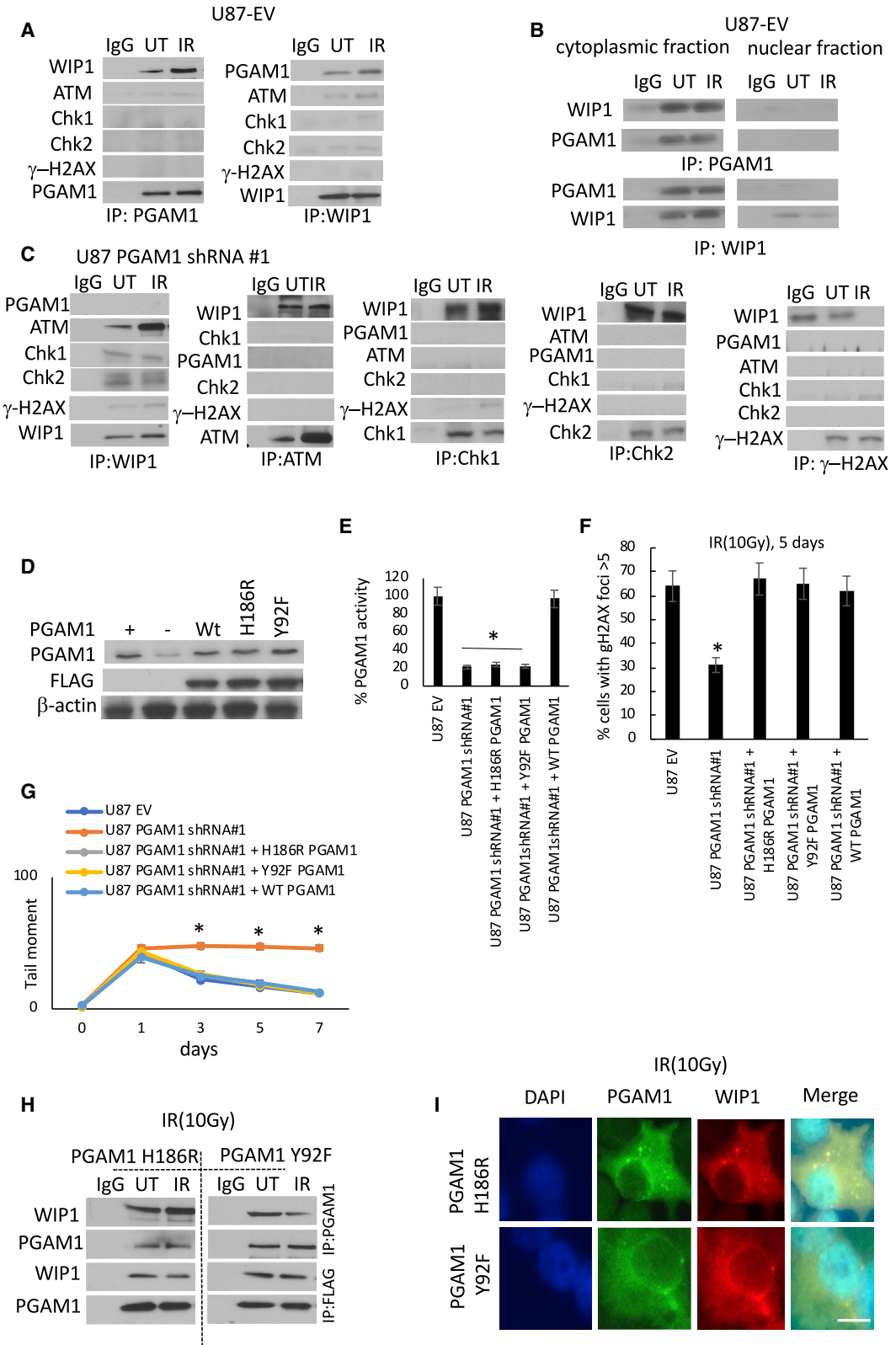

(legend on next page)

survival in mice carrying tumors expressing catalytic inactive Y92F and H186R PGAM1 mutants, as seen in animals harboring PGAM1-deficient tumors (Figure 7B). Upon pathological examination, PGAM1 knockdown tumors treated with IR and TMZ were indeed significantly smaller in size compared with corresponding time-matched vehicle-treated tumors (Figure 7C, top panel). U87 PGAM1 shRNA#1 tumors treated with IR and TMZ had a decreased proliferative index (MIB1, 22% ± 3.3% and 26% ± 4.5%, respectively; Figure 7C), whereas the untreated U87 PGAM1 shRNA#1 tumors had a higher proliferative index (59.4% ± 6.8%). Cleaved caspase-3 levels were elevated in PGAM1 knockdown tumors treated with IR (33% ± 4.7%) and TMZ (27% ± 5.1%) compared with vehicle-treated (2% ± 4.3%) tumors. In summary, inhibition of PGAM1 restricted growth of human GBMs within the intracranial environment in response to IR and TMZ, with decreased proliferation but enhanced apoptosis. These results show that loss of PGAM1 sensitizes glioma cells to IR and TMZ treatment *in vivo*, similar to the effects of PGAM1 loss *in vitro*.

DISCUSSION

During cancer initiation and progression, alterations to different metabolic enzymes promote neoplastic transformation (Hsu and Sabatini, 2008; Vander Heiden and DeBerardinis, 2017; Keibler et al., 2016). Adding to evidence from previous studies, the present study shows that same level of PGAM1 overexpression occurs at every grade (I–IV) of glioma. Moreover, this study demonstrates that PGAM1 overexpression blocks the deactivation of the DDR pathway, which makes these cells treatment resistant to different DNA-damaging agents. In normal cells, the DDR pathway becomes activated whenever there is DNA damage resulting in sequential events of (1) recognition of the damage site, (2) activation of the DDR pathway, (3) cell-cycle arrest, and finally (4) deactivation of the DDR pathway (Kim and Haber, 2009).

In these sequential events, PGAM1 overexpression in glioma appears to play role in blocking the deactivation of the DDR pathway, thereby making it constitutively active and providing resistance against IR- and TMZ-mediated DNA damage. In this study, IR and TMZ treatment produced similar levels of DNA damage in both parental cells and PGAM1-knockdown cells, but PGAM1-knockdown cells exhibited inefficient repair as observed by fewer γ-H2AX foci, which indicated a decrease in initiation of the DDR pathway. Control of DNA repair pathway activation and deactivation is regulated in a variety of ways, including through regulators of the metabolic processes. Previous work demonstrated the role of PGAM1 in DNA double-strand break repair by HR through regulation of CtIP (Qu et al., 2017). This study showed that genetic silencing or pharmacological inhibition of PGAM1 in HeLa cells results in CtIP protein degradation and p53/p73 pathway activation (Qu et al., 2017). In normal cells, DNA damage results in the formation of DDR foci, which leads to cell-cycle arrest due to the presence of intact cell cycle checkpoints, followed by efficient repair, and finally disassembly of the DDR foci removes the break from cell cycle progression. In contrast, deregulation of cell proliferation is an early step in tumorigenesis that elicits DNA replication stress and ongoing DNA damage formation, which results in activation of the DDR pathway, specifically activation of the downstream ATM and ATR pathways characterized by phosphorylation of ATM, Chk1, Chk2, and γ-H2AX. (Bartkova et al., 2005, 2010; Gorgoulis et al., 2005). But despite DDR activation, as these tumorigenic cells do not have effective cell cycle checkpoints, cell-cycle arrest does not occur, and these cells with defective DNA replicate, thus increasing genomic instability. On the other hand, constitutively active and efficient DDR provides a common mechanism for cancer therapy resistance. As such, it has been reported that glioma stem cells display an efficient DDR pathway and are refractory to radiation treatment (Bao et al., 2006).

In normal cells, deactivation of DDR foci can occur in a variety of ways after repair is completed. Reversing PARylation, a post-translational change, can lead to dissociation of DDR foci (Gagné et al., 2006). Yeast Pph3, PP1 (Keogh et al., 2006; Bazzi et al., 2010), and mammalian PP1, PP2A, PP4, PP6, and WIP1 (Nazarov et al., 2003; Chowdhury et al., 2005; Nakada et al., 2008; Cha et al., 2010; Douglas et al., 2010; Macůrek et al., 2010; Moon et al., 2010Chowdhury et al., 2008), and Tip60 phosphatases in human and *Drosophila* cells can reverse the phosphorylation of γ-H2AX (Kusch et al., 2004; Jha et al., 2008). Our present study reveals that PGAM1 overexpression appears to contribute to the

Figure 5. WT and Kinase-Dead PGAM1 Physically Interact with WIP1 and Thereby Block Binding with ATM, Chk1, Chk2, and γ-H2AX

(A) Western blot analysis of levels of PGAM1, WIP1, Chk1, Chk2, and γ-H2AX was performed in PGAM1, WIP1, and IgG immunoprecipitates from control U87 cells with and without IR treatment.

(B) Western blot analysis of WIP1 and PGAM1 was performed in PGAM1, WIP1, and IgG immunoprecipitates from the nuclear (N) and cytoplasmic (C) fractions of parental U87 cells with and without IR (10 Gy) treatment.

(C) Western blot analysis of levels of PGAM1, WIP1, Chk1, Chk2, and γ-H2AX was performed in PGAM1, WIP1, and IgG immunoprecipitates from PGAM1-knockdown U87 cells with and without IR treatment.

(D) Western blot analysis of levels of PGAM1 and FLAG expression in PGAM1 shRNA-expressing U87 cells expressing FLAG-tagged WT and two kinase-dead mutant forms (H186R and Y92F) of PGAM1. Western blot analysis of β-actin (bottom of panel) was used to verify equal input.

(E) PGAM1 activity (mean + SE) of cells from (D) was determined in triplicate for each group using an assay coupled to the oxidation of NADH.

(F) Quantitative analysis of γ-H2AX foci counted on >200 cells per group from (D), following immunofluorescent staining with anti-Ser-139-phosphorylated γ-H2AX antibody (in red) and counterstained with DAPI (in blue) to visualize nuclei.

(G) Analysis of tail moment (a measure of DNA fragmentation) in cells from (D) treated with IR (10 Gy) and harvested after 0, 1, 3, 5, and 7 days. Each point represents the mean + SE of at least 100 cells per treatment.

(H) Western blot analysis of levels of PGAM1 and WIP1 was performed in PGAM1, FLAG, and IgG immunoprecipitates in PGAM1 shRNA-expressing U87 cells expressing two FLAG tagged kinase-dead mutant forms (H186R and Y92F) of PGAM1 with and without IR treatment.

(I) DAPI (blue)/PGAM1 (green)/WIP1 (red) co-immunofluorescence analysis was used in PGAM1-knockdown U87 that was rescued with two FLAG tagged kinase-dead mutant forms (H186R and Y92F) of PGAM1. Scale bars, 10 μm.

Except where noted, all values were derived from three independent experiments ± SD. *$p < 0.05$.

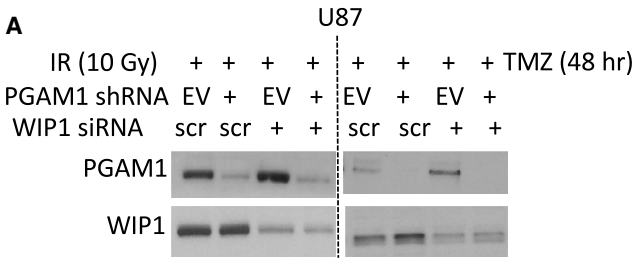

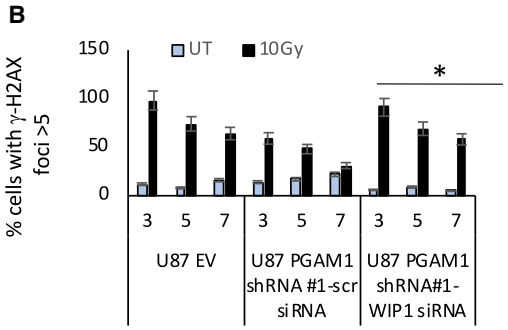

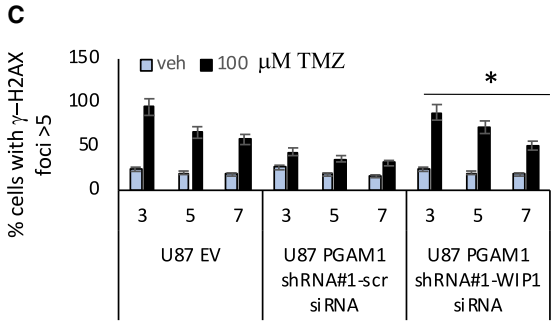

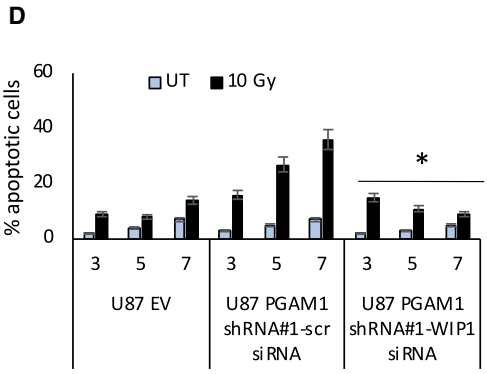

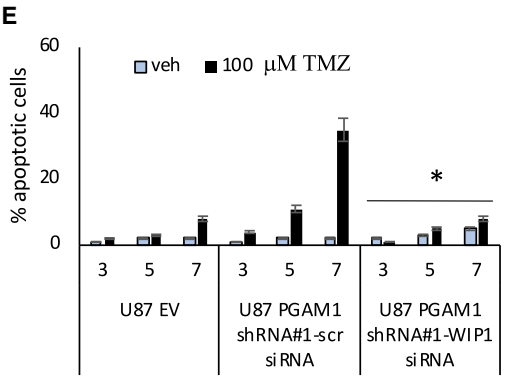

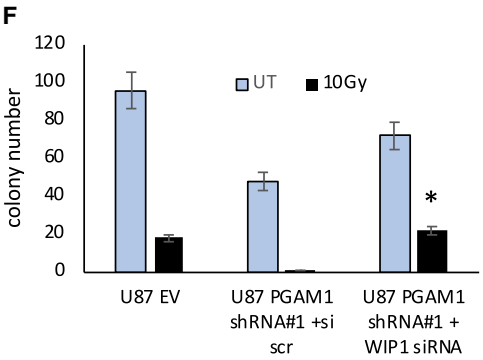

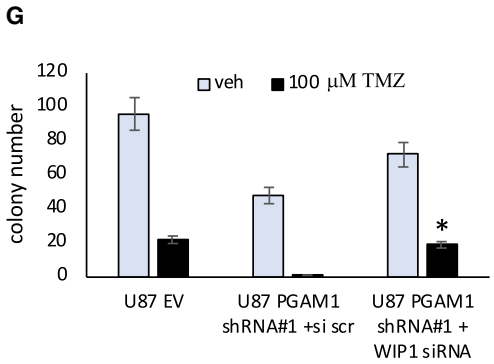

(legend on next page)

constitutive activation of the DDR pathway by inhibiting a natural phosphatase, WIP1, which in normal cells deactivates important DDR pathway proteins by dephosphorylating them. Per previous studies, p53 is one of the transcriptional activators of WIP1 and DNA damage may lead to the activation of p53, followed by elevated WIP1 activation that downregulates downstream DNA damage sensing pathway (Fiscella et al., 1997). In our system, we did not observe any change in expression of WIP1 after DNA-damaging treatment (IR and TMZ) in p53 WT U87 cells or in LN319 cells that have been reported to have a mutation in p53 (Van Meir et al., 1994). These observations indicate that the link among DNA damage, p53 activation, and WIP1 regulation is not prominent in the context of glioma. Moreover, previous literature suggests PGAM1 as a negative transcription target of p53 (Kondoh et al., 2005), and we found overexpression of PGAM1 in both p53 WT U87 cells as well as p53-mutated LN319 cells. A contradictory study demonstrated that in rat cardiomyocyte, p53 upregulates expression of PGAM1 (Ruiz-Lozano et al., 1999). Our present study demonstrates a p53-independent role of WIP1 and PGAM1 expression in glioma cells.

Our results advance the current understanding of how PGAM1 regulates the subcellular localization of WIP1 and thereby regulates its DDR-related activity. PGAM1 is mostly a cytoplasmic protein that directly interacts with WIP1 and keeps it in the cytoplasm. As a result, WIP1 is unable to travel to the nucleus and is not able to deactivate ATM, Chk1, Chk2, and γ-H2AX by dephosphorylation (Figure 7C). Although the aforementioned findings provide a potentially crucial link between PGAM1 and treatment resistance through the DDR system via WIP1 regulation, the linkage is clearly context dependent. In PGAM1-overexpressing glioma cells, WIP1 is expressed at the normal physiological level. In this scenario, normal physiological levels of WIP1 most likely control only the DDR pathway proteins and not the proteins involved in other pathways (e.g., p53, p38, NF-κb, ER-α, c-Jun, E2F1) (Lowe et al., 2012). Conversely there are tumors that express high levels of WIP1, which then regulate other pathways along with DDR pathway. Knocking down WIP1 overexpression has been reported to alter ATM signaling and activate the DDR pathway (Lowe et al., 2012). Most likely, not all overexpressed WIP1 can bind with PGAM1 (even if PGAM1 is also overexpressed), resulting in free WIP1 to perform other functions in addition to DDR regulation. In gliomas, as WIP1 is not overexpressed, and genetically modifying its expression only results in changes to the DDR pathway, this strongly suggests that the functional activity of normal physiological expression of WIP1 is to regulate the DDR pathway (Lowe et al., 2012). When it is overexpressed, it regulates several other pathways (such as stress-induced, NER, and inflammatory pathways) (Lowe et al., 2012), and in that setting genetic or pharmacological inhibition of WIP1 may have different functional outcome.

As shown before, the enzymatic role of PGAM1 can be metabolic or non-metabolic in nature (Hitosugi et al., 2012; Qu et al., 2017). But as a protein, PGAM1 was shown to interact with ACTA2 (Zhang et al., 2017) and control migration of cancer cells. Similarly, our work demonstrates WIP1 as a direct interacting partner of PGAM1. Also, we showed that this interaction is independent of the enzymatic activity of PGAM1. Tumors that overexpress PGAM1 not only have accordingly high activity of this metabolic enzyme but would also possess increased suppression of WIP1 function through the non-enzymatic, non-metabolic role of PGAM1 in interacting with WIP1. This activation of the DDR pathway is shown herein to be very efficient in making glioma cells resistant to standard therapy such as IR and TMZ chemotherapy.

The non-metabolic control of the DDR pathway supports the idea that the enzymes involved in the cellular bioenergetics pathway actually regulate a wider spectrum of events than was not previously appreciated. This non-metabolic role of PGAM1 acts as a switch for constitutive activation of the DDR pathway that promotes therapeutic resistance and can be exploited by using appropriate inhibitors that can block its interaction with WIP1, combined with DNA-damaging agents. We have demonstrated that downregulation of PGAM1 expression sensitizes glioma cells toward TMZ and IR, thereby increasing the efficiency of the standard therapeutic regimen for the treatment of glioma. The present findings have implications not only for our understanding of how PGAM1 overexpression contributes to glioma growth but also for therapy for PGAM1-overexpressing tumors.

STAR★METHODS

Detailed methods are provided in the online version of this paper and include the following:

- KEY RESOURCES TABLE
- RESOURCE AVAILABILITY
  - Lead Contact
  - Materials Availability
  - Data and Code Availability
- EXPERIMENTAL MODEL AND SUBJECT DETAILS

Figure 6. Silencing of WIP1 in PGAM-Knockdown Cells Rescues IR and TMZ Sensitivity

(A) Levels of WIP1 and β-actin in cells from Figure 2A transfected with a non-targeted (Scr-siRNA-) or a pooled mixture of five siRNAs targeting WIP1 and treated with IR (10 Gy) or TMZ (100 μM).

(B) Quantitative analysis of phospho-γ-H2AX foci counted on >200 cells per group. The percentage of cells with phospho-γ-H2AX foci was determined in all cell populations treated with IR (10 Gy) at the indicated time points.

(C) Quantitative analysis of phospho-γ-H2AX foci counted on >200 cells per group as indicated. The percentage of cells with phospho-γ-H2AX foci was determined in all cell populations treated with TMZ (100 μM) at the indicated time points.

(D and E) Apoptosis in glioma cells from (A) with and without IR (10 Gy) (D) and (E) with and without TMZ (100 μM) treatment was measured using annexin V staining and flow cytometry analysis after 3, 5, or 7 days of treatment.

(F and G) Number of colonies (>50 cells) that arose in soft agar 28 days following plating of the cells from (A) with and without IR (10 Gy) treatment (F) and (G) with and without TMZ (100 μM) treatment.

Except where noted, all values were derived from three independent experiments ± SD. *$p < 0.05$.

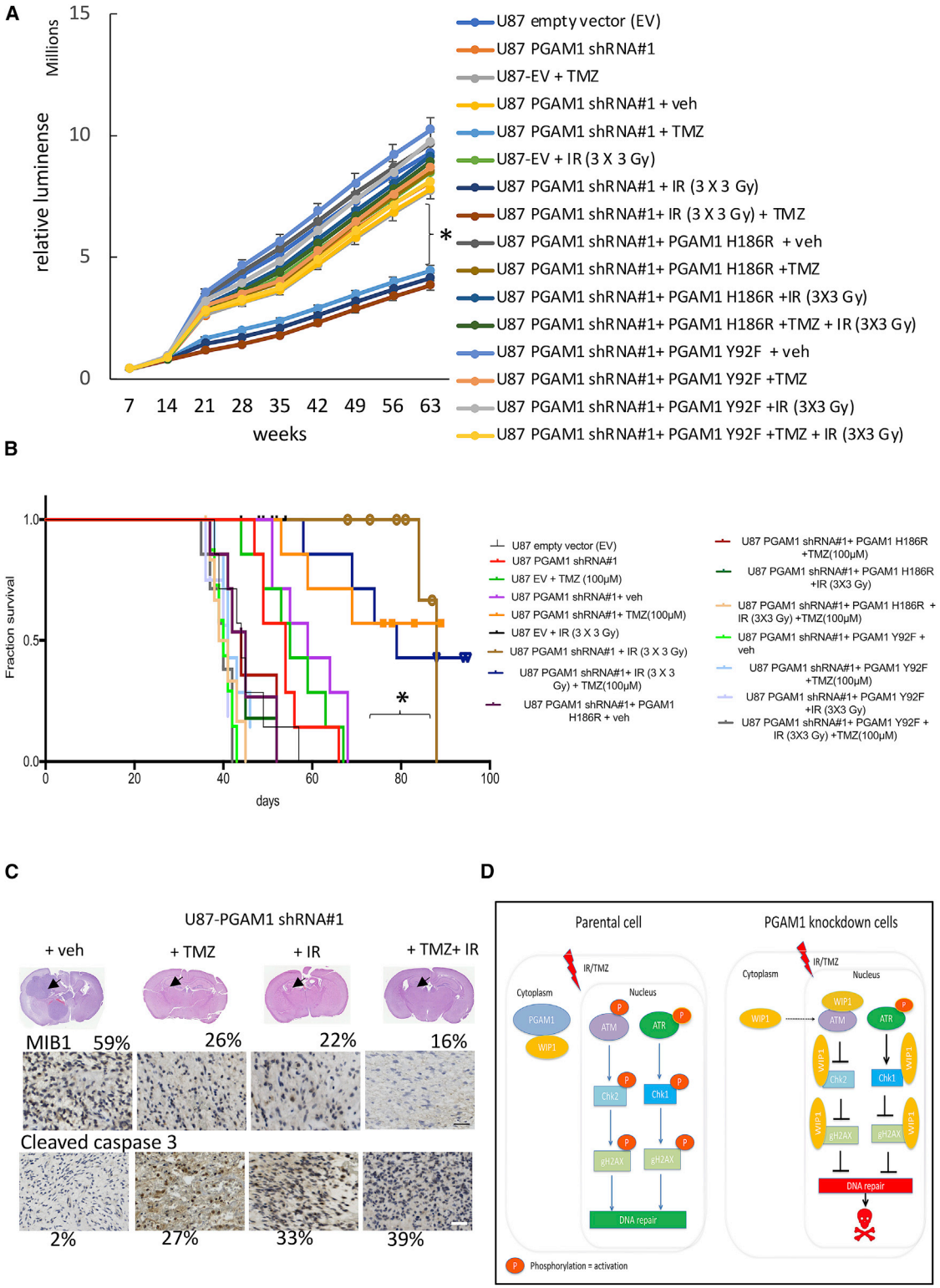

Figure 7. Knocking Down PGAM1 Increases TMZ/IR Sensitivity in Glioma Xenografts

(A) *In vivo* growth curves of orthotopic, bioluminescence-labeled control, stable PGAM1-silenced, and PGAM1-silenced U87 tumor cells stably expressing one of two FLAG-tagged kinase-dead mutant forms (H186R and Y92F) of PGAM1. Three weeks post-implantation, the animals were treated with vehicle (DMSO), IR (10 Gy), TMZ (100 μM), or both IR (10 Gy) and TMZ (100 μM). Data are mean ± SD. *$p < 0.05$, $n = 7$.

(legend continued on next page)

SUPPLEMENTAL INFORMATION

Supplemental Information can be found online at https://doi.org/10.1016/j.celrep.2020.03.082.

ACKNOWLEDGMENTS

We thank Wendy See and Ilona Garner for their diligent proofreading of this paper. This work was supported in part by National Institutes of Health grant NS105087-02 (R.O.P.) and The Kristian Gerhard Jebsen Foundation (to T.-C.A.J.).

AUTHOR CONTRIBUTIONS

S.O., T.-C.A.J., R.O.P., and J.M. designed the experiments. S.O. and T.-C.A.J. equally performed the experiments with the help of K.C. and X.Y. T.-C.A.J. and J.M. wrote the paper.

DECLARATION OF INTERESTS

The authors declare no competing interests.

Received: May 29, 2019
Revised: December 18, 2019
Accepted: March 25, 2020
Published: April 14, 2020

REFERENCES

Bao, S., Wu, Q., McLendon, R.E., Hao, Y., Shi, Q., Hjelmeland, A.B., Dewhirst, M.W., Bigner, D.D., and Rich, J.N. (2006). Glioma stem cells promote radioresistance by preferential activation of the DNA damage response. Nature *444*, 756–760.

Barritault, M., Meyronet, D., and Ducray, F. (2018). Molecular classification of adult gliomas: recent advances and future perspectives. Curr. Opin. Oncol. *30*, 375–382.

Bartkova, J., Horejsí, Z., Koed, K., Krämer, A., Tort, F., Zieger, K., Guldberg, P., Sehested, M., Nesland, J.M., Lukas, C., et al. (2005). DNA damage response as a candidate anti-cancer barrier in early human tumorigenesis. Nature *434*, 864–870.

Bartkova, J., Hamerlik, P., Stockhausen, M.T., Ehrmann, J., Hlobilkova, A., Laursen, H., Kalita, O., Kolar, Z., Poulsen, H.S., Broholm, H., et al. (2010). Replication stress and oxidative damage contribute to aberrant constitutive activation of DNA damage signalling in human gliomas. Oncogene *29*, 5095–5102.

Bazzi, M., Mantiero, D., Trovesi, C., Lucchini, G., and Longhese, M.P. (2010). Dephosphorylation of gamma H2A by Glc7/protein phosphatase 1 promotes recovery from inhibition of DNA replication. Mol. Cell. Biol. *30*, 131–145.

Capello, M., Ferri-Borgogno, S., Cappello, P., and Novelli, F. (2011). α-Enolase: a promising therapeutic and diagnostic tumor target. FEBS J. *278*, 1064–1074.

Certo, M.T., Ryu, B.Y., Annis, J.E., Garibov, M., Jarjour, J., Rawlings, D.J., and Scharenberg, A.M. (2011). Tracking genome engineering outcome at individual DNA breakpoints. Nat. Methods *8*, 671–676.

Cha, H., Lowe, J.M., Li, H., Lee, J.S., Belova, G.I., Bulavin, D.V., and Fornace, A.J., Jr. (2010). Wip1 directly dephosphorylates gamma-H2AX and attenuates the DNA damage response. Cancer Res. *70*, 4112–4122.

Cheung, E.C., and Vousden, K.H. (2010). The role of p53 in glucose metabolism. Curr. Opin. Cell Biol. *22*, 186–191.

Chowdhury, D., Keogh, M.C., Ishii, H., Peterson, C.L., Buratowski, S., and Lieberman, J. (2005). γ-H2AX dephosphorylation by protein phosphatase 2A facilitates DNA double-strand break repair. Mol. Cell *20*, 801–809.

Chowdhury, D., Xu, X., Zhong, X., Ahmed, F., Zhong, J., Liao, J., Dykxhoorn, D.M., Weinstock, D.M., Pfeifer, G.P., and Lieberman, J. (2008). A PP4-phosphatase complex dephosphorylates gamma-H2AX generated during DNA replication. Mol. Cell *31*, 33–46.

Curtin, N.J. (2013). Inhibiting the DNA damage response as a therapeutic manoeuvre in cancer. Br. J. Pharmacol. *169*, 1745–1765.

DeBerardinis, R.J., and Chandel, N.S. (2016). Fundamentals of cancer metabolism. Sci. Adv. *2*, e1600200.

Douglas, P., Zhong, J., Ye, R., Moorhead, G.B., Xu, X., and Lees-Miller, S.P. (2010). Protein phosphatase 6 interacts with the DNA-dependent protein kinase catalytic subunit and dephosphorylates gamma-H2AX. Mol. Cell. Biol. *30*, 1368–1381.

Engel, M., Mazurek, S., Eigenbrodt, E., and Welter, C. (2004). Phosphoglycerate mutase derived polypeptide inhibits glycolytic flux and induces cell growth arrest in tumor cell lines. J. Biol. Chem. *279*, 35803–35812.

Evans, M.J., Saghatelian, A., Sorensen, E.J., and Cravatt, B.F. (2005). Target discovery in small-molecule cell-based screens by in situ proteome reactivity profiling. Nat. Biotechnol. *23*, 1303–1307.

Fiscella, M., Zhang, H., Fan, S., Sakaguchi, K., Shen, S., Mercer, W.E., Vande Woude, G.F., O'Connor, P.M., and Appella, E. (1997). Wip1, a novel human protein phosphatase that is induced in response to ionizing radiation in a p53-dependent manner. Proc. Natl. Acad. Sci. U S A *94*, 6048–6053.

(B) Kaplan-Meier survival curves for animals (N = 7 for each group) intracranially implanted with U87-empty vector (EV), U87-PGAM1 shRNA#1, and U87-PGAM1 shRNA-H186R-FLAG and U87-PGAM1 shRNA-Y92F-FLAG cells followed by treatment with vehicle (veh; DMSO), IR (10 Gy), TMZ (100 μM), or both IR (10 Gy) and TMZ (100 μM).
(C) Top panel: representative photomicrograph of hematoxylin and eosin-stained section of U87-PGAM1 shRNA tumors. Scale bars, 2,000 μm. Arrow points to the tumors in all groups. Middle and bottom panels, histopathology of U87-PGAM1 shRNA intracranial tumors with antibodies specific to MIB1 (scale bar, 100 μm) and cleaved caspase-3 (scale bar, 100 μm), respectively. The percentages of proliferating cells (MIB1) and apoptotic cells (cleaved caspase-3) are indicated above and below the representative photomicrographs, respectively.
(D) Schematic overview of the proposed mechanism of PGAM1-mediated DNA damage repair pathway regulation through WIP1 binding in the cytoplasm.

Fouse, S.D., Nakamura, J.L., James, C.D., Chang, S., and Costello, J.F. (2014). Response of primary glioblastoma cells to therapy is patient specific and independent of cancer stem cell phenotype. Neuro Oncol. *16*, 361–371.

Gagné, J.P., Hendzel, M.J., Droit, A., and Poirier, G.G. (2006). The expanding role of poly(ADP-ribose) metabolism: current challenges and new perspectives. Curr. Opin. Cell Biol. *18*, 145–151.

Gorgoulis, V.G., Vassiliou, L.V., Karakaidos, P., Zacharatos, P., Kotsinas, A., Liloglou, T., Venere, M., Ditullio, R.A., Jr., Kastrinakis, N.G., Levy, B., et al. (2005). Activation of the DNA damage checkpoint and genomic instability in human precancerous lesions. Nature *434*, 907–913.

Hartwell, L.H., and Kastan, M.B. (1994). Cell cycle control and cancer. Science *266*, 1821–1828.

Hitosugi, T., Zhou, L., Elf, S., Fan, J., Kang, H.B., Seo, J.H., Shan, C., Dai, Q., Zhang, L., Xie, J., et al. (2012). Phosphoglycerate mutase 1 coordinates glycolysis and biosynthesis to promote tumor growth. Cancer Cell *22*, 585–600.

Hitosugi, T., Zhou, L., Fan, J., Elf, S., Zhang, L., Xie, J., Wang, Y., Gu, T.L., Alečković, M., LeRoy, G., et al. (2013). Tyr26 phosphorylation of PGAM1 provides a metabolic advantage to tumours by stabilizing the active conformation. Nat. Commun. *4*, 1790.

Hsu, P.P., and Sabatini, D.M. (2008). Cancer cell metabolism: Warburg and beyond. Cell *134*, 703–707.

Ito, M., Ohba, S., Gaensler, K., Ronen, S.M., Mukherjee, J., and Pieper, R.O. (2013). Early Chk1 phosphorylation is driven by temozolomide-induced, DNA double strand break- and mismatch repair-independent DNA damage. PLoS ONE *8*, e62351.

Jha, S., Shibata, E., and Dutta, A. (2008). Human Rvb1/Tip49 is required for the histone acetyltransferase activity of Tip60/NuA4 and for the downregulation of phosphorylation on H2AX after DNA damage. Mol. Cell. Biol. *28*, 2690–2700.

Jiang, X., Sun, Q., Li, H., Li, K., and Ren, X. (2014). The role of phosphoglycerate mutase 1 in tumor aerobic glycolysis and its potential therapeutic implications. Int. J. Cancer *135*, 1991–1996.

Keibler, M.A., Wasylenko, T.M., Kelleher, J.K., Iliopoulos, O., Vander Heiden, M.G., and Stephanopoulos, G. (2016). Metabolic requirements for cancer cell proliferation. Cancer Metab. *4*, 16.

Keogh, M.C., Kim, J.A., Downey, M., Fillingham, J., Chowdhury, D., Harrison, J.C., Onishi, M., Datta, N., Galicia, S., Emili, A., et al. (2006). A phosphatase complex that dephosphorylates gammaH2AX regulates DNA damage checkpoint recovery. Nature *439*, 497–501.

Kim, J.A., and Haber, J.E. (2009). Chromatin assembly factors Asf1 and CAF-1 have overlapping roles in deactivating the DNA damage checkpoint when DNA repair is complete. Proc. Natl. Acad. Sci. U S A *106*, 1151–1156.

Kondoh, H., Lleonart, M.E., Gil, J., Wang, J., Degan, P., Peters, G., Martinez, D., Carnero, A., and Beach, D. (2005). Glycolytic enzymes can modulate cellular life span. Cancer Res. *65*, 177–185.

Kusch, T., Florens, L., Macdonald, W.H., Swanson, S.K., Glaser, R.L., Yates, J.R., 3rd, Abmayr, S.M., Washburn, M.P., and Workman, J.L. (2004). Acetylation by Tip60 is required for selective histone variant exchange at DNA lesions. Science *306*, 2084–2087.

Liu, Z.G., Ding, J., Du, C., Xu, N., Wang, E.L., Li, J.Y., Wang, Y.Y., and Yu, J.M. (2018). Phosphoglycerate mutase 1 is highly expressed in C6 glioma cells and human astrocytoma. Oncol. Lett. *15*, 8935–8940.

Lowe, J., Cha, H., Lee, M.-O., Mazur, S.J., Appella, E., and Fornace, A.J., Jr. (2012). Regulation of the Wip1 phosphatase and its effects on the stress response. Front. Biosci. *17*, 1480–1498.

Macůrek, L., Lindqvist, A., Voets, O., Kool, J., Vos, H.R., and Medema, R.H. (2010). Wip1 phosphatase is associated with chromatin and dephosphorylates gammaH2AX to promote checkpoint inhibition. Oncogene *29*, 2281–2291.

Mancini, A., Xavier-Magalhães, A., Woods, W.S., Nguyen, K.T., Amen, A.M., Hayes, J.L., Fellmann, C., Gapinske, M., McKinney, A.M., Hong, C., et al. (2018). Disruption of the β1L isoform of GABP reverses glioblastoma replicative immortality in a TERT promoter mutation-dependent manner. Cancer Cell *34*, 513–528.

Moon, S.H., Lin, L., Zhang, X., Nguyen, T.A., Darlington, Y., Waldman, A.S., Lu, X., and Donehower, L.A. (2010). Wild-type p53-induced phosphatase 1 dephosphorylates histone variant gamma-H2AX and suppresses DNA double strand break repair. J. Biol. Chem. *285*, 12935–12947.

Mukherjee, J., Phillips, J.J., Zheng, S., Wiencke, J., Ronen, S.M., and Pieper, R.O. (2013). Pyruvate kinase M2 expression, but not pyruvate kinase activity, is up-regulated in a grade-specific manner in human glioma. PLoS ONE *8*, e57610.

Mukherjee, J., Ohba, S., See, W.L., Phillips, J.J., Molinaro, A.M., and Pieper, R.O. (2016). PKM2 uses control of HuR localization to regulate p27 and cell cycle progression in human glioblastoma cells. Int. J. Cancer *139*, 99–111.

Mukherjee, J., Johannessen, T.C., Ohba, S., Chow, T.T., Jones, L., Pandita, A., and Pieper, R.O. (2018). Mutant IDH1 cooperates with ATRX loss to drive the alternative lengthening of telomere phenotype in glioma. Cancer Res. *78*, 2966–2977.

Nakada, S., Chen, G.I., Gingras, A.C., and Durocher, D. (2008). PP4 is a gamma H2AX phosphatase required for recovery from the DNA damage checkpoint. EMBO Rep. *9*, 1019–1026.

Nazarov, I.B., Smirnova, A.N., Krutilina, R.I., Svetlova, M.P., Solovjeva, L.V., Nikiforov, A.A., Oei, S.L., Zalenskaya, I.A., Yau, P.M., Bradbury, E.M., and Tomilin, N.V. (2003). Dephosphorylation of histone gamma-H2AX during repair of DNA double-strand breaks in mammalian cells and its inhibition by calyculin A. Radiat. Res. *160*, 309–317.

Pavlova, N.N., and Thompson, C.B. (2016). The emerging hallmarks of cancer metabolism. Cell Metab. *23*, 27–47.

Qu, J., Sun, W., Zhong, J., Lv, H., Zhu, M., Xu, J., Jin, N., Xie, Z., Tan, M., Lin, S.H., et al. (2017). Phosphoglycerate mutase 1 regulates dNTP pool and promotes homologous recombination repair in cancer cells. J. Cell Biol. *216*, 409–424.

Ruiz-Lozano, P., Hixon, M.L., Wagner, M.W., Flores, A.I., Ikawa, S., Baldwin, A.S., Jr., Chien, K.R., and Gualberto, A. (1999). p53 is a transcriptional activator of the muscle-specific phosphoglycerate mutase gene and contributes in vivo to the control of its cardiac expression. Cell Growth Differ. *10*, 295–306.

Sanzey, M., Abdul Rahim, S.A., Oudin, A., Dirkse, A., Kaoma, T., Vallar, L., Herold-Mende, C., Bjerkvig, R., Golebiewska, A., and Niclou, S.P. (2015). Comprehensive analysis of glycolytic enzymes as therapeutic targets in the treatment of glioblastoma. PLoS ONE *10*, e0123544.

Van Meir, E.G., Kikuchi, T., Tada, M., Li, H., Diserens, A.-C., Wojcik, B.E., Huang, H.-J.S., Friedmann, T., de Tribolet, N., and Cavenee, W.K. (1994). Analysis of the p53 gene and its expression in human glioblastoma cells. Cancer Res. *54*, 649–652.

Vander Heiden, M.G., and DeBerardinis, R.J. (2017). Understanding the intersections between metabolism and cancer biology. Cell *168*, 657–669.

Vander Heiden, M.G., Locasale, J.W., Swanson, K.D., Sharfi, H., Heffron, G.J., Amador-Noguez, D., Christofk, H.R., Wagner, G., Rabinowitz, J.D., Asara, J.M., and Cantley, L.C. (2010). Evidence for an alternative glycolytic pathway in rapidly proliferating cells. Science *329*, 1492–1499.

Wolf, A., Agnihotri, S., Micallef, J., Mukherjee, J., Sabha, N., Cairns, R., Hawkins, C., and Guha, A. (2011). Hexokinase 2 is a key mediator of aerobic glycolysis and promotes tumor growth in human glioblastoma multiforme. J. Exp. Med. *208*, 313–326.

Zhang, D., Jin, N., Sun, W., Li, X., Liu, B., Xie, Z., Qu, J., Xu, J., Yang, X., Su, Y., et al. (2017). Phosphoglycerate mutase 1 promotes cancer cell migration independent of its metabolic activity. Oncogene *36*, 2900–2909.

STAR★METHODS

KEY RESOURCES TABLE

REAGENTS OR RESOURCES	SOURCE	IDENTIFIER
Antibodies		
PARP	Cell signaling	MA3-950
PGAM1	Cell signaling	sc-7212
caspase-3	Cell signaling	sc-966
g-H2AX	Millipore	05-636
pATM s1981	Cell signaling	13050
ATM	Cell signaling	2873
pChk2 thr68	Cell signaling	2197
Chk2	Santa Cruz	sc-5278
pChk1 s-345	Cell signaling	2348
Chk1	Cell signaling	2360
pcdc25c s-216	Cell signaling	4901
cdc-25C	Santa Cruz	sc13138
p-Ser/Thr	Abcam	ab117253
ATR	Cell signaling	2790
WIP1	Cell signaling	11901
Histone H3	Cell signaling	4499
b-tubulin	Cell signaling	2146
FLAG	SIGMA	F3165-.2MG
PP1	Santa Cruz	sc-7482
PP2A	Santa Cruz	sc-80665
PP4	R&D systems	MAB5074
PP6	Santa Cruz	sc-393294
MIB1	DAKO	M724001-2
cleaved caspase 3	Cell signaling	9661
ACTA2	Abcam	ab7817
CtIP	Santa Cruz	sc-271339
Chemicals, Peptides, and Recombinant proteins		
Alizarin	Selleck	S2526
PGAMtide	New England Peptide	Custom made
DAPI	Invitrogen	D1306
protein A/G PLUS - agarose beads	Santa Cruz	sc-2003
Critical Commercial Assays		
Alamar Blue reagent	Invitrogen	DAL1100
Comet assay kit	Trevigen, Gaithersburg, MD	4250-050-K
MycoSensor Mycoplasma Detection PCR Assay Kit	Agilent Technologies	302108
Annexin-V staining Kit	BD PharMingen	556547
Experimental Models: Cell Lines		
NHA	Lonza	CC-2565
U87	ATCC	ATCC HTB-14
LN319	UCSF Brain Tumor Center	N/A
U251	ATCC	N/A
SF10602	UCSF Brain Tumor Center	N/A

(*Continued on next page*)

Continued

REAGENTS OR RESOURCES	SOURCE	IDENTIFIER
SF7976	UCSF Brain Tumor Center	N/A
SF8279	UCSF Brain Tumor Center	N/A
Experimental Models: Organisms/Strains		
nu/nu mice	Charles River	strain-490
Oligonucleotides		
siWIP1	Dharmacon	ON-TARGETplus SMARTpool siRNA J-003546-13, TERF2
si scr	Dharmacon	siGenome non-targeting siRNA pool#2, 5nmol
siPP1	Santa Cruz biotechnology	sc-43545
siPP2A	Santa Cruz biotechnology	sc-43509
siPP4	Santa Cruz biotechnology	sc-62848
si PP6	Santa Cruz biotechnology	sc-96346
si scr	Santa Cruz biotechnology	sc-37007
shPGAM1#1	IDT	shPGAM1#1, 5′-CCATCCTTTCTACAGCAACAT-3′
shPGAM1#2	IDT	shPGAM1#2, 5′-CCTGTGAGAGTCTGAAGGATA-3′
Recombinant DNA		
pcDNA3:FLAG	Addgene	#20011
pcDNA3:Flag: PGAM1	This paper	pcDNA3:PGAM1
pcDNA3:Flag: PGAM1H186R	This paper	pcDNA3:Flag: PGAM1H186R
pcDNA3:Flag: PGAM1Y92F	This paper	pcDNA3:Flag: PGAM1Y92F
WT PGAM1-shRNA#1 resistant	Qu J et al. Vol. 216 No. 2, February 1, 2017.	WT PGAM1-shRNA#1 resistant
Software and Algorithms		
Metamorph Imaging Software	Molecular Devices	N/A
PRISM	Graph Pad	N/A

RESOURCE AVAILABILITY

Lead Contact

Please contact J.M. (joydeep.mukherjee@ucsf.edu) for reagents and resources generated in this study.

Materials Availability

All unique/stable reagents generated in this study are available from the Lead Contact without restriction

Data and Code Availability

This study did not generate any unique datasets or code.

EXPERIMENTAL MODEL AND SUBJECT DETAILS

Cell culture

The human glioma cell lines U87, U251, LN319, SF10601, SF7996 and SF8279 were provided by the UCSF Brain Tumor Center Tissue Core. All cells were cultured as described (Mukherjee et al., 2016; Mukherjee et al., 2013; Fouse et al., 2014; Mancini et al., 2018), identities were confirmed by short tandem repeat analysis (Promega Geneprint Kit), confirmed mycoplasma negative (MycoSensor Mycoplasma Detection PCR Assay Kit; Agilent Technologies), and used within 3 passages of thawing.

Animal model

4 weeks old female Immunodeficient mice (nu/ nu; Charles River) were caged (5 animals/cage) and maintained with standard rodent chow diet and water *ad libitum*, under a 12 h light/dark cycle at constant temperature and humidity. The animals were monitored daily

and were sacrificed once neurological symptoms developed and reached the end point as described in the animal protocol. The guidelines of the UCSF Institutional Animal Care and Use Committee were followed for all animal work.

Human samples

Non-tumor brain tissue samples were obtained from autopsy (N = 2) or from cancer-free epilepsy patients who underwent temporal lobe resection (N = 3). Formalin-fixed paraffin embedded sections were used for neuropathological verification of tumor grade based on the WHO classification scheme (Barritault et al., 2018) and identified grade I (juvenile pilocytic astrocytoma, N = 2, adult pilocytic astrocytoma, N = 3), grade II (diffuse astrocytoma, N = 5), grade III (anaplastic astrocytoma, N = 5), and grade IV (glioblastoma, N = 5) specimens. All 25 samples (15 male and 10 female, between the age range of 9 −70 years.) were obtained from the UCSF Brain Tumor Research Center Tissue Core (University of California, San Francisco) using protocols approved by the UCSF Institutional Review Board. DNA, mRNA and protein were isolated from corresponding frozen and fixed sections that contained greater than 75% non-necrotic tumor tissue.

METHOD DETAILS

Real-time PCR

Total-RNA was extracted (RNeasy Kit, QIAGEN), dissolved in nuclease-free water, and analyzed (Agilent 2100 Bioanalyzer). Real-time PCR was performed in triplicate to measure PGAM1, WIP1, and β-actin mRNA levels. For PGAM1, the 1st set of primers were forward 5- GGAGGGGAAACGTGTACTGA-3, reverse 5- CAGAGAGACCCTCCAGATGC-3 and 2nd set of primers were forward 5′- AACCATGCTAAGCCATGACC-3′ and reverse 5′- GCAGTGACCTGACTGCAGAA-3.'' For WIP1, the primers were 5-CTGT ACTCGCTGGGAGTGAG-3 and 5-GTTCGGGCTCCACAACGATT-3. For β-actin the primers were 5-GATGAGATTGGCAT GGCTTT-3 and 5- CACCTTCACCGTTCCAGTTT-3. Thermal cycling conditions consisted of an initial step of 95°C for 3 minutes followed by 40 cycles at 95°C for 15 s, 60°C for 15 s, and 72°C for 30 s (Rotor Gene, QIAGEN).

Modulation of PGAM1 and WIP1 expression

Empty shRNA vectors (EV) or one of two different lentiviral PGAM1 shRNAs, were used to transduce U87 and LN319 cells as described (Mukherjee et al., 2016; Mukherjee et al., 2013). Parental and PGAM1 knock-down cells were subsequently either transiently transfected (Fugene 6) with pooled siRNA targeting WIP1 (Dharmacon), PP1, PP2A, PP4 and PP6 (Santa Cruz biotechnology) or transduced with lentiviral constructs encoding three different forms of human FLAG-tagged PGAM1 (WT-shRNA resistant, kinase-dead PGAM1 H186R, and kinase-dead PGAM1 Y92F). In each case the appropriate scrambled shRNA and siRNA were also used. Coding sequences of FLAG-PGAM1 and indicated mutants were cloned to pCDNA3.1 vector. Nonsense point mutations to the underlined nucleotides 5′-CCACCCATTTTACAGCAACAT-3′ in the corresponding coding sequence of PGAM1 in the pCDNA3.1 plasmid confer resistance to shRNA#1 silencing. WT or mutant PGAM1 reconstituted cells were stable lines generated by Lipofectamine 2000 (Invitrogen) transfection followed by G418 selection. The monoclones used in this study had a comparable expression as like endogenous PGAM1.

Cell growth assays

Three thousand cells per well were plated onto 96-well plates and cultured overnight in 100 μL of media. Media contained vehicle, PGAM-tide (MRQIKIWFPNRRMKWKKHHHHHHPWLIRHGE), control peptide (MRQIKIWFPNRRMKWKKHHHHHHPWRIEGHL) (50) (synthesized from New England Peptide **Gardner, MA),** and alizarin (60 μM) for 5 days. Cells were then treated with 20 μL Alamar Blue reagent (Invitrogen) per well for one hour and fluorescence (A540/620) was measured using a Synergy 2 Multi-mode Microplate reader (BioTek Instruments). Percent cell growth was determined by normalizing fluorescence measurements to media-only controls.

PGAM1 activity assay

U87 and LN319 cells were grown to 25% confluency and were harvested. Soluble proteomes were prepared in 30 mM Tris-HCl (pH 7.0) and tested for PGAM1 activity by monitoring the conversion of 3-phosphoglyceric acid to 2-phosphoglyceric acid at 20°C–25°C using an assay coupled to the oxidation of NADH as described by Evans et al., 2015.

Oxidative PPP flux assay

Oxidative PPP flux was measured as described previously (Hitosugi et al., 2012). Briefly, cells were seeded on 60 mm dishes within a 100 mm dish that is completely sealed to collect the ^{14}CO2 release from a pinhole. The cells were incubated in 2 mL of medium containing [1-14C]- or [6-14C]-glucose, respectively, at a final specific activity of 10 μCi/ml glucose at 37°C for 3 h. By injecting 0.3 mL of 50% TCA from another pinhole oxidative PPP flux was stopped and 0.3 mL of Hyamine Hydroxide was injected to trap $^{14}CO_2$ release by placing a small cup. Hyamine Hydroxide was dissolved into 60% methanol and subjected to scintillation counting.

3-PG assay

Cells were homogenized in 1.5mL lysis buffer to determine the concentration of 3-PG as described previously (Hitosugi et al., 2012). The supernatant from the homogenate were collected by centrifugation at 4°C for 10 minutes at 16,000 rpm and were applied to

Amicon Ultra tubes filter (10KDa cut off, Millipore). NADH, ADP, $MgCl_2$, recombinant LDH and PKM1 proteins were added to the flow that contain the metabolites at a final concentration of 0.14 mM, 1 mM, 50 mM, 5 μg/ml and 10 μg/ml respectively. Recombinant enolase protein was added to a final concentration of 50 μg/ml to measure cellular 2-PG. Once the reaction was initiated by enolase, a decrease in absorbance at 340nm from NADH oxidation was measured by a Synergy 2 Multi-mode Microplate reader (BioTek Instruments). Recombinant PGAM1 was added (final conc. 25ug/ml) after termination of the enolase reaction and immediately monitored for the absorbance (340nm) to measure cellular 3-PG.

Cell cycle distribution, apoptosis, soft agar assay, and DNA damage foci studies

a. Cell cycle distribution analysis: For cell cycle distribution, fixed, propidium iodide-labeled cells were subjected to flow cytometry using a FACSCalibur (BD Biosciences). Cell cycle and sub-G1 analysis was performed using Flowjo software (Treestar).
b. Apoptosis analysis: For apoptosis analysis, an Annexin-V staining Kit was used (BD PharMingen) and analyzed as per the manufacturer's instructions.
c. Soft agar assay: Soft agar assays were performed as previously described (‘). Numbers of colonies (> 50 cells) and average diameter of the colonies for each condition were measured on 100 × photomicrographs and analyzed using Metamorph Imaging Software (Molecular Devices).
d. DNA damage foci analysis: DNA damage foci analysis was carried out by the use of -H2AX-specific primary antibodies (1:200), and fluorescent-tagged secondary antibodies. Fluorescence microscopy was performed on > 200 cells per group, and the percentage of cells with -H2AX foci (red foci) was determined as described (Mukherjee et al., 2018).

IHC analysis

Immunohistochemistry was performed on a Ventana Medical Systems Benchmark XT using anti-human PGAM1 (1:250 dilution, 60 min, Abcam), MIB1(1:100, DAKO), cleaved caspase-3 (1:50, Cell Signaling Technology) antibody. Staining was visualized using 3, 3′-Diaminobenzidine tetrahydrochloride (Ventana). Negative and positive controls were included in each run. PGAM1 staining was scored using a four-tier scale: 0, no immunostaining; 1, > 0% to ≤ 10% positive; 2, > 10% to ≤ 25% positive; 3, > 25% to ≤ 75%; and 4, > 75% tumor cells positive. Ki-67 and cleave caspase-3 staining was scored. The proliferating and apoptotic index (percentage) was calculated as the number of positive nuclei over total nuclei.

Comet assay

The DNA damage in the cells was measured using a Comet assay kit (Trevigen, Gaithersburg, MD) according to the manufacturer's protocol. As described previously (Ito et al., 2013), after trypsinization and PBS wash, the cells were suspended in a low-temperature-melting agarose and immediately layered onto Comet Slides (Trevigen). Thirty-minute incubation at 4°C allowed the agarose to set. Then the slides were directly subjected to electrophoresis in neutral buffer before being immersed in DNA precipitation solution for 30 minutes at room temperature. After electrophoresis, the slides were dried, stained using SYBR Green (Trevigen), and observed by fluorescent microscope. One hundred cells per treatment were analyzed using the computer-based image analysis system (Comet Assay, Perceptive Instruments Ltd.). The amount of DNA double strand breaks was quantitated and expressed as the ‘‘tail moment,’’ which combined a measurement of the length of the DNA migration and the relative DNA content.

Cell fractionation, protein extraction, immunoprecipitation, and western blot analysis

Protein lysates from control or PGAM1 knockdown cells and subfractions (NE-PER Extraction kit, Pierce) were prepared in lysis buffer supplemented with protease and phosphatase inhibitors (Roche). For immunoprecipitation, protein lysates were precleared with protein A/G-agarose beads (Santa Cruz, 3 hours, 4°C), and then incubated with primary antibody (16 hours, 4°C). Immune complexes were precipitated (2 hours, 4°C) with protein A/G-agarose beads. In control samples, the primary antibody was substituted with control IgG. Immunoprecipitates were washed four times with RIPA buffer containing 0.5 M NaCl and 2% SDS, washed three times with PBS, and then resuspended in Laemmli buffer. Proteins were separated on 4%–20% gradient polyacrylamide gels and transferred onto Immuno-Blot PVDF membranes (Bio-Rad Laboratories). Membranes were then incubated in blocking buffer (1X TBS containing 5% milk and 0.05% Tween-20, 2 hours), and probed overnight with antibodies specific for the cytoplasmic marker β-tubulin (1:1000), the nuclear marker histone H3 (1:1000), PGAM1 (1:1000), β-actin (1:20,000), WIP1 (1:1000), caspase-3,(1:1000), PARP (1:1000), pATM (1:2000), ATM, pChk1 (1:2000), Chk1 (all Cell Signaling), pChk2, Chk2 (1:1000), pcdc25C(1:500)(Santa Cruz), phospho Ser/Thr, ATR, (1:500)(Abcam), PP1, PP2A, PP6, (Santa Cruz) PP4 (Abcam), CtIP(Abcam) and ACTA2 (Santa Cruz) and washed, then incubated with appropriate horseradish peroxidase-conjugated secondary antibodies (Santa Cruz Biotechnology). Antibody binding was detected by incubation with ECL reagents (Amersham Pharmacia Biotech).

ATR activity assay

Cell lysates from parental and PGAM1 knockdown cells were generated 6 hours after TMZ treatment as described previously (Ito et al., 2013). Briefly, the lysate was sonicated, incubated overnight at 4°C with an antibody targeting ATR or IgG, and then precipitated with agarose A/G beads (1 hour, 4°C). The beads were washed and then incubated, and the reaction products were separated on a

15% SDS-polyacrylamide gel and subjected to immunoblotting with anti-phospho-serine threonine substrate antibody (Cell Signaling) or anti-ATR (Santa Cruz) goat polyclonal antibodies to assure equivalent kinase abundance.

Immunofluorescence staining

Cultured cells grown overnight in 4-well chambered slides were fixed in paraformaldehyde (4%, 10 minutes). For antigen unmasking, slides were placed in 1 mM EDTA pH 8 (10 minutes, 100°C under pressure) followed by 15 min at a sub-boiling temperature. After rinsing twice in PBST, all slides were blocked (3% normal goat serum and 0.2% Triton X-100 in PBS, 30 min, room temperature), and then incubated with PGAM1 (1:200) and WIP1 (1:100) primary antibodies in 1% goat serum and 0.2% Triton X-100 in PBS (18–20 hours, 4°C). After washing, slides were incubated with fluorescent-tagged secondary antibodies (647, 588, 1:200, 2 hours, Invitrogen) appropriate for the host species of the primary antibody. Following washing (PBS, 3x5 min each), sections were incubated with DAPI, washed, and mounted. Negative controls for antibody labeling were performed by omitting primary or secondary antibodies.

In vivo *studies*

Immunodeficient mice (nu/ nu; Charles River) (n = 7 in each group) were injected intracranially with 4×10^5 luciferase-expressing U87-empty vector (EV), U87-PGAM1 shRNA#1, U87-PGAM1 shRNA -H186R-FLAG, U87-PGAM1 shRNA and U87-PGAM1 shRNA -Y92F-FLAG cells. Tumor growth was monitored weekly by treating mice with D-luciferin (150 mg/kg IP, Gold- Biotechnology) and measuring bioluminescence using a Xenogen IVIS Bioluminescence imaging station (Caliper). Tumor growth was calculated by normalizing luminescence measurements to Day 1 post-injection values. Three weeks after implantation, the animals were treated with vehicle (veh, DMSO); IR (3Gy each on 21^{st},28^{th} and 35^{th} day post tumor cell implantation) or TMZ (5mg/kg dissolved in ora plus q.d. from 21st-25th and 35^{th}-40^{th} day post tumor cell implantation). The animals were monitored daily for any neurological signs and were sacrificed once symptoms developed and reached the end point as described in the animal protocol. Kaplan–Meir survival curves were generated by plotting days of survival following implantation. The guidelines of the UCSF Institutional Animal Care and Use Committee were followed for all animal work.

Measurement of homologous recombination (HR) and non-homologous end joining (NHEJ) efficiency:

HR and NHEJ efficiency of the parental and PGAM1 knockdown cells was evaluated using the Traffic Light Reporter (TLR) system (Certo et al., 2011). pCVL Traffic Light Reporter 1.1 (SceI target) EF1 Puro and pCVL-SFFVd14GFP EF1sHA.NLS.Sce (opt) were a gift from A.Scharenberg (Addgene plasmid #31482 and #31476). We performed assays using U87 and LN319 parental and PGAM1 knockdown cells that were stably integrated with TLR construct, which if repaired accurately by HR using the provided HR donor sequence after ISceI mediated cut will results in green signals from intact GFP sequence or if undergoes NHEJ then will generate red signal from mCherry sequence. The cells were co-transfected with DNA plasmids containing an HR donor and ISceI enzyme. At 3 days post treatment, cells were analyzed by flow cytometry. Data shown are normalized with non-transduced control cells (not infected with ISceI carrying virus). ATM inhibitor Ku55933 and DNA ligase-4 inhibitor SCR7 (SelleckChemicals) was used as a positive control for HR and NHEJ inhibition respectively (53).

QUANTIFICATION AND STATISTICAL ANALYSIS

Data are reported as mean ± standard error of at least three experiments. When two groups were compared, the unpaired Student's t test was applied. When multiple groups were evaluated, the one-way ANOVA test with post hoc Tukey–Kramer multiple comparisons test was used. $p < 0.05$ was considered statistically significant.